

# THREE-DIMENSIONAL SIMULATIONS OF DISK ACCRETION TO INCLINED DIPOLE: I. MAGNETOSPHERIC FLOW AT DIFFERENT $\Theta$

M.M. ROMANOVA

Department of Astronomy, Cornell University, Ithaca, NY 14853-6801; romanova@astro.cornell.edu

G.V. USTYUGOVA

Keldysh Institute of Applied Mathematics, Russian Academy of Sciences, Moscow, Russia;  
ustyugg@spp.Keldysh.ru

A.V. KOLDOBA

Institute of Mathematical Modelling, Russian Academy of Sciences, Moscow, Russia;  
koldoba@spp.Keldysh.ru

J.V. WICK

Department of Astronomy, Cornell University, Ithaca, NY 14853-6801; jvw3@cornell.edu

R.V.E. LOVELACE

Department of Astronomy, Cornell University, Ithaca, NY 14853-6801; rv11@cornell.edu

*Subject headings:* accretion, dipole — plasmas — magnetic fields — stars: magnetic fields — X-rays: stars

*Draft version November 8, 2018*

## ABSTRACT

We present results of fully three-dimensional magnetohydrodynamic (MHD) simulations of disk accretion to a slowly rotating magnetized star with its dipole moment inclined at an angle  $\Theta$  to the rotation axis of the disk (which is assumed to be aligned with the spin axis of the star). The main goal was to investigate the pattern of magnetospheric flow and the disk-star interaction for a variety of inclination angles  $\Theta$ . We observed that at  $\Theta = 0^\circ$ , the disk stops at magnetospheric radius  $r_m$ , and matter flows to the star through axisymmetric funnel flows, as observed in earlier axisymmetric simulations. However, when the dipole moment of the star is inclined, then the flow becomes non-axisymmetric. The non-axisymmetry becomes notable at very small inclination angles  $\Theta \sim 2^\circ - 5^\circ$ . The pattern of magnetospheric flow is different at different  $\Theta$ . For relatively small angles,  $\Theta \lesssim 30^\circ$ , the densest matter flows to the star mostly in two streams, which follow paths to the closest magnetic pole. The streams typically co-rotate with the star, but they may precess about the star for  $\Theta \lesssim 10^\circ$ . At intermediate angles,  $30^\circ \lesssim \Theta \lesssim 60^\circ$ , the streams become more complicated, and often split into four streams. For even larger angles,  $\Theta \gtrsim 60^\circ$ , matter accretes in two streams, but their geometry is different from the streams at small  $\Theta$ . Magnetic braking changes the structure of the inner regions of the disk. It creates a region of lower density (a “gap”) for  $r_m \lesssim r \lesssim 4r_m$ . A ring of higher density forms at  $r \sim r_m$  for  $\Theta \lesssim 30^\circ$ . For  $r \lesssim (2-3)r_m$ , the azimuthal velocities are sub-Keplerian. The inner region of the disk at  $r \sim r_m$  is warped. The warping is due to the tendency of matter to co-rotate with inclined magnetosphere. The normal of the inner warped part of the disk is close to the magnetic axis of the dipole. The accreting matter brings positive angular momentum to the (slowly rotating) star tending to spin it up. The corresponding torque  $N_z$  depends only weakly on  $\Theta$ . The angular momentum flux to the star near the star’s surface is transported predominantly by the magnetic field; the matter component contributes  $\sim 1\%$  of the total flux. The torques  $N_x$  and  $N_y$  are also calculated and these may give a slow precession of the symmetry axis of the star. The angle  $\Theta$  was fixed in simulations because the time scale of its evolution is much longer than that of the simulations. Results of simulations are important for understanding the nature of classical T Tauri stars, cataclysmic variables, and X-ray pulsars. These stars often show complicated spectral and photometric variability patterns, which may be connected with the structure of magnetospheric flows. The magnetospheric structure of stars with different  $\Theta$  can give different variability patterns in observed light curves. This can provide information about inclination angles  $\Theta$  in different stars. A notable result of the present simulations is the formation of multiple streams in the accretion flows near the star for intermediate inclination angles. This may give short-scale quasi-periodic variability in the light curves of some stars.

## 1. INTRODUCTION

*1.1. Observations.* Disk accretion to a rotating star with a dipole magnetic field is important in a number of objects, including classical T Tauri stars, cataclysmic variables and X-ray binaries. Commonly, the magnetic axis of the dipole is not aligned with the rotation axis of the disk. The disk

accretion to rotating neutron stars with misaligned dipole fields gives rise to X-ray pulsars in binary systems (see, e.g., Trümper et al. 1985; Sheffer et al. 1992; Bildsten et al. 1997; Deeter et al. 1998). The periodic variability in some cataclysmic variables is thought to be due to the rotation of a star with a misaligned dipole field (e.g., Livio

& Pringle 1992; Warner 1995; Warner 2000; Wickramasinghe, Wu, & Ferrario 1991). A similar cause may give the photometric and spectral variability of some classical T Tauri stars (e.g., Herbst et al. 1986; Bouvier & Bertout 1989; Johns & Basri 1995; Hartmann 1998; Bouvier, et al. 1999, 2003; Petrov, et al. 2001).

Disk accretion to an inclined dipole rotator occurs in different systems. For specificity we adopt a scaling of the parameters appropriate for classical T Tauri Stars (CTTSs). Application to other objects such as neutron stars may be done by rescaling the parameters.

Following the discovery of variability of classical T Tauri stars (CTTSs) (Herbst et al. 1986; Bertout et al. 1988), it was suggested that this variability may be due to rotational modulation of emission of “hot spots” on the surface of the star which are connected with magnetospheric funnel flows (Camenzind 1990; Königl 1991). Many observations of CTTSs support this model. In some cases (e.g., AA Tau), the variability may be due to the warp of the inner part of the disk (Bouvier et al. 1999, 2003). Photometric and spectral variability of CTTSs often shows complicated patterns which have not been explained. In order to understand the nature of the variability of different CTTSs, it is important to calculate the detailed MHD flow pattern in the magnetosphere outside of the inclined rotator. The magnetic field of CTTSs may not be a pure dipole (e.g., Safier 1998, Smirnov et al. 2003). However, this paper considers the case where the star’s field is a dipole field.

*1.2. Theory of Disk Accretion to an Inclined Rotator.* The problem of disk accretion to an inclined dipole rotator has been investigated theoretically by a number of authors. These works considered the the possible warping of the inner part of the disk.

It was noticed in 1970s that in case of diamagnetic disk (when magnetic field does not penetrate the disk) the magnetic pressure will be different above and below the disk so that there is a net force perpendicular to the disk. This force causes warping of the disk (Scharlemann 1978; Aly 1980). This early work considered the case in which the rotational axis of the distant disk  $\Omega_d$  and spin of the star  $\Omega_*$  coincide. Later, the analysis was extended to the case in which the  $\Omega_d$  and  $\Omega_*$  are in different directions (Lipunov & Shakura 1980; Lipunov, Semenov & Shakura 1981; Horn & Kundt 1989; Lai 1999). The net force acting on the inner regions of the disk (averaged over the rotation of the star) acts so as to make the normal to the warped disk perpendicular to both the magnetic axis of the dipole and spin of the star. The disk is expected to precess around the spin axis of the star. Subsequently, Lai (1999) extended this analysis to cases of imperfectly conducting disks. Later, it was shown that *viscosity* may decrease warping (Horn & Kundt 1989; Lai 1999). Agapitou, Papaloizou & Terquem (1997) and Terquem & Papaloizou (2000) conclude that bending waves may also lead to warping, and the amplitude of the warp will depend on viscosity parameter  $\alpha$ .

The theoretical models typically involve a number of simplifying approximations. Predictions of these models should be checked numerically. This paper, however, does not focus on this topic, and no special simulations were arranged to enhance the warping.

No theories were done on the main topic of this paper

- analysis of magnetospheric flows in the inclined magnetosphere. This problem is principally three-dimensional and needs full 3D simulations. Some of the important problems, however, were investigated analytically and numerically in an axisymmetric approach, which is valuable for subsequent 3D analysis.

*2.3. 2D Simulations of the Disk-Star Interaction.* Different aspects of the disk-star interaction for the case of an aligned rotator were investigated with two-dimensional, axisymmetric MHD simulations (Hayashi, Shibata & Matsumoto 1996; Miller & Stone 1997; Hirose et al. 1997). Special attention was given to the problem of opening of the coronal magnetic field lines and associated outflows (Goodson, Böhm & Winglee 1999; Fend & Elstner 2000). This process was earlier investigated theoretically by Lovelace, Romanova, & Bisnovaty-Kogan (1995), and Bardou & Heyvaerts (1996). Much less attention has been given to numerical investigation of the dipole interaction with the inner regions of the disk and modelling of magnetospheric flows, which were investigated analytically by Ghosh & Lamb (1979a,b), Shu et al. (1994), Ostriker & Shu (1995), Wang (1995), Li & Wickramasinghe (1997), Koldoba et al. (2002a), and others. This problem was not fully investigated by MHD simulations because of the difficulty of creating consistent “quiescent initial conditions.” In most simulations the initial magnetic braking of the disk by the magnetospheric field leads to the fast accretion of disk matter to the star with velocity close to free-fall (e.g., Hayashi et al. 1996; Miller & Stone 1997). Furthermore, the strong initial twist forms at the boundary between the disk and corona, and this acts to initiate outflows.

Romanova et al. (2002, hereafter R02) developed consistent quiescent initial conditions, which lead to slow, viscous time-scale accretion avoiding the free-fall accretion of earlier studies. This opened up the possibility of investigating the physics of the disk-star interaction and magnetospheric flows in great detail on the viscous time-scale. Many aspects of the earlier predicted theories were reconsidered (R02). It was shown that (1) the magnetic field lines in the inner regions of the disk have a tendency to be closed, while external lines may be open (see also recent paper by Küker, Henning, Rüdiger 2003); (2) the inner regions of the disk experience magnetic braking and their angular velocity is smaller/larger than Keplerian (depending on angular velocity of the star); (3) the magnetic field is dominant in the spinning-up/spinning-down of the star; (4) the main force lifting matter up to the funnel flow is the pressure gradient force, while magnetic force is negligibly small. Different aspects of earlier proposed models were confirmed or rejected. With detailed axisymmetric analysis in hand, it was easier to undertake the three-dimensional MHD simulations of the disk accretion to the inclined dipole.

In order to understand accretion to a misaligned rotator, we created a special three-dimensional MHD simulation code based on a “cubed sphere” grid. This grid has a number of advantages over spherical or Cartesian grids (Koldoba et al. 2002b, hereafter K02). A similar grid was developed for the surface of the sphere for geophysical applications (see, e.g., Ronchi, Iacono, & Paolucci 1996). In contrast with these authors, we perform simulations in the three-space and use as a base the Godunov-type numer-

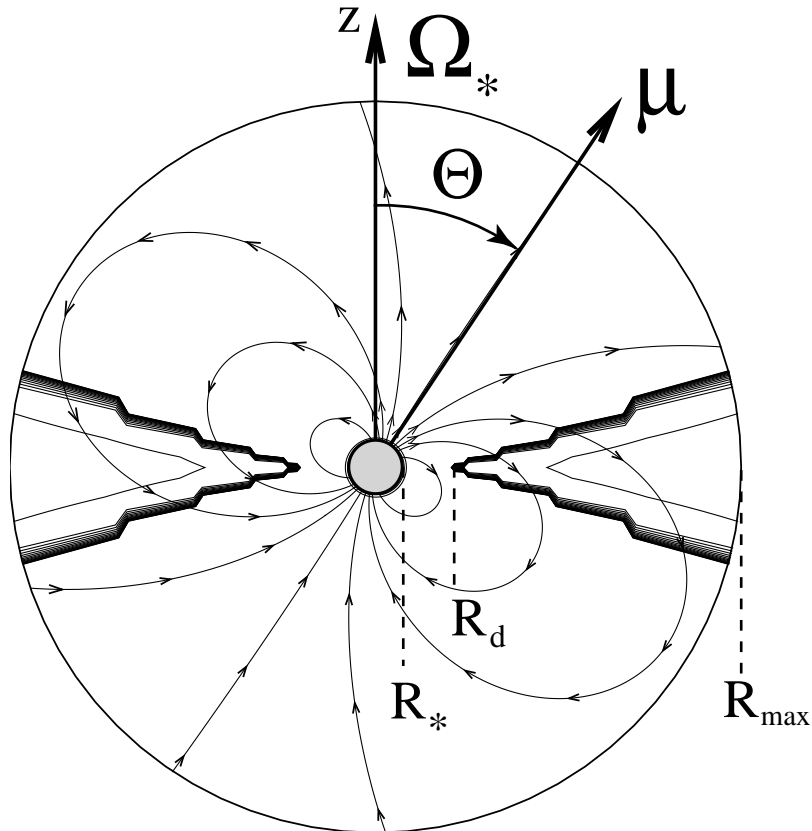


FIG. 1.— Initial conditions for simulations. A star of radius  $R_*$  is threaded with the dipole magnetic field with the magnetic momentum  $\mu$  inclined relative to the  $z$ -axis at an angle  $\Theta$ .  $R_{\max}$  - is the size of the simulations region. The solid lines with arrows represent magnetic field lines. The level lines of the disk are shown. The inner radius of the disk is located at  $R_d$ .

ical scheme which is similar to one described by Powell et al. (1999). We performed sample simulations of three-dimensional accretion to an inclined rotator for an inclination angle  $\Theta = 30^\circ$  and obtained the first interesting results. We observed that after one rotation of the inner radius of the disk, the initial axisymmetry of the disk is destroyed, and matter flows to the star along two streams.

In this paper we present the results for the full range of inclination angles  $\Theta$ . The main goals of the simulations are the following: (1) to investigate the structure of the magnetospheric flows at different inclination angles  $\Theta$ , which is important for subsequent analysis of spectral and photometric variability of CTTs and other stars; (2) to investigate the properties of the disk surrounding the magnetosphere; (3) to investigate the rate of spinning up/down of the star and its dependence on  $\Theta$ ; and (4) to investigate how inclination angles  $\Theta$  may change with time. In future papers we will show detailed analysis of the 3D streams and hot spots, and will derive the light curves from simulations (Romanova et al. 2004a).

In §2, the numerical model is described. In §3, test simulations are presented. In §4, the main numerical results for different  $\Theta$  are discussed. In §5, the magnetic braking of the disk is analyzed. In §6, the fluxes of matter and torque to the star are calculated. In §7, the main conclusions of this work are presented and the possible observational consequences are discussed.

## 2. NUMERICAL MODEL

We investigate the case in which the angular velocity of the star  $\Omega = \Omega_*$  and that of the disk are aligned and in the  $\hat{z}$  direction. The magnetic moment  $\mu$  is inclined relative to  $\hat{z}$  axis by an angle  $\Theta$  as shown in Figure 1. We fix inclination angle  $\Theta$  and do not change it during simulations, thus reflecting the fact that the angular momentum of the star is much larger than the angular momentum of accreting matter. In general, the angular momenta of the star and that of the disk may be misaligned, but in the present paper we consider only the aligned case. The initial magnetic field is considered to be a dipole field,  $\mathbf{B} = 3(\mu \cdot \mathbf{R})\mathbf{R}/R^5 - \mu/R^3$ . We use a reference frame  $(X, Y, Z)$  rotating with the star with the  $Z$  axis aligned with the star's rotation axis. This rotating frame is orientated such that  $\mu$  is in the  $(X, Z)$  plane.

We solve the system of ideal MHD equations. We decompose the magnetic field  $\mathbf{B}$  into the “main” dipole component of the star  $\mathbf{B}_0$ , and the component,  $\mathbf{B}_1$ , induced by currents in the disk and in the corona. This helps to minimize errors in calculating the magnetic force (e.g., Tanaka 1994). In the case of the inclined rotating dipole the dipole moment changes with time. It rotates with angular velocity  $\Omega$  so that the “main” field  $\mathbf{B}_0$  also changes with time. Consequently in the induction equation there is a large term involving  $\mathbf{B}_0$ . To overcome this difficulty

we use a coordinate system rotating with angular velocity  $\mathbf{\Omega}$ , in which the magnetic moment of the star  $\boldsymbol{\mu}$  and the “main” field  $\mathbf{B}_0$  do not depend on time. The system of MHD equations in the coordinate system rotating with the star is

$$\frac{\partial \rho}{\partial t} + \nabla \cdot (\rho \mathbf{v}) = 0, \quad (1)$$

$$\frac{\partial (\rho \mathbf{v})}{\partial t} + \nabla \cdot T = \rho \mathbf{g} + 2\rho \mathbf{v} \times \mathbf{\Omega} - \rho \mathbf{\Omega} \times (\mathbf{\Omega} \times \mathbf{R}), \quad (2)$$

$$\frac{\partial (\rho s)}{\partial t} + \nabla \cdot (\rho s \mathbf{v}) = 0, \quad (3)$$

$$\frac{\partial \mathbf{B}}{\partial t} = \nabla \times (\mathbf{v} \times \mathbf{B}), \quad (4)$$

(K02) where  $\rho$  is the plasma density,  $s$  is the entropy,  $T_{ik}$  is the stress tensor with  $T_{ik} = p\delta_{ik} + \rho v_i v_k + (\mathbf{B}^2 \delta_{ik}/2 - B_i B_k)/4\pi$ . Here  $\mathbf{v}$  is the velocity of plasma in the rotating frame. The transformation to the inertial (observer’s) frame is  $\mathbf{u} = \mathbf{v} + \mathbf{\Omega} \times \mathbf{R}$ . One can see that equation (2), which is the Euler equation in the rotating frame, has new terms compared to the usual Euler equation, namely, the Coriolis and centrifugal forces. The Godunov-type numerical code was used in the “cubed sphere” coordinate system. The code was tested and verified to give the correct solution for Bondi accretion to a gravitating object with a monopole magnetic field (K02).

### 2.1. Reference Values and Example for T Tauri Stars

The reference value for distance is denoted  $R_0$ , and it is taken to be the initial value of the inner radius of the disk. Thus the dimensionless inner disk radius is  $R_d = 1$  initially. We take the dimensionless radius of the star to be  $R_* = 0.35$ . The reference value for the velocity is taken to be the Keplerian velocity at  $R_0$ ,  $v_0 = (GM/R_0)^{1/2}$ . The reference angular rotation rate is  $\omega_0 = v_0/R_0$ , and the corresponding time-scale is  $t_0 = R_0/v_0$ . We also use the rotation period at  $r = R_0$ ,  $P_0 = 2\pi t_0$ . For a given magnetic field strength at  $R_0$  we can define a reference density as  $\rho_0 = B_0^2/v_0^2$  and reference pressure  $p_0 = \rho v_0^2$ . A reference magnetic moment of the star is then  $\mu_0 = B_0 R_0^3$ . Thus, the calculated variables are:  $R' = R/R_0$ ,  $t' = t/t_0$ ,  $\rho' = \rho/\rho_0$ ,  $v' = v/v_0$ ,  $B' = B/B_0$ ,  $p' = p/p_0$ . We also introduce the dimensionless time,  $T = t/P_0$ . Subsequently, the primes are dropped, but the physical values can easily be restored for a particular case.

Here, we discuss the numerical parameters for a typical T Tauri star. We take the mass and radius of the star to be  $M = 0.8M_\odot$  and  $R_* = 1.8R_\odot$ . Our reference length is approximately equal to the inner radius of the disk  $R_0 \approx 2.86R_* \approx 3.6 \times 10^{11}$  cm. The reference velocity is  $v_0 \approx 1.93 \times 10^7$  cm/s, and the corresponding time-scale is  $t_0 \approx R_0/v_0 \approx 1.89 \times 10^4$  s. The size of the simulation region corresponds to  $R_{\max} = 0.34$  AU. The period of Keplerian rotation of the inner radius of the disk is  $P_0 \approx 1.38$  days.

Consider  $B_* = 10^3$  G at the surface of the star. Then at  $R = R_0$ , the reference magnetic field is  $B_0 = B_*(R_*/R_0)^3 \approx 42.7$  G and the reference magnetic moment is  $\mu_0 = B_0 R_0^3 \approx 2.0 \times 10^{36}$  Gcm<sup>3</sup>. The reference density is  $\rho_0 = 4.89 \times 10^{-12}$  g/cm<sup>3</sup> or  $n = 3.06 \times 10^{12}$  cm<sup>-3</sup> which is typical for T Tauri star disks. The reference mass accretion rate is  $\dot{M}_0 = \rho_0 v_0 R_0^2 \approx 1.2 \times 10^{19}$  g/s  $\approx 1.92 \times 10^{-7} M_\odot/\text{year}$ .

### 2.2. Initial and Boundary Conditions

To derive the initial distribution of density and pressure in the disk and corona, we use *quiescent* initial conditions which were developed for our axisymmetric two-dimensional (R02) and test three-dimensional simulations (K02). The main idea for creation of quiescent initial conditions was: (1) to minimize the initial magnetic braking between the slowly rotating dipole and matter of the disk rotating with Keplerian velocity, and (2) to minimize the effect of the rapid twisting of the magnetic field between the disk and corona as a result of the fast turn on of the disk rotation. The first process typically leads to fast accretion of matter in the disk with a velocity close to free-fall, while the second process leads to the formation of a strong  $B_\phi$  component near the disk and a transient matter outburst to the corona (e.g., Hayashi et al. 1996; Miller & Stone 1997). To minimize these factors, we had the corona rotate with the Keplerian velocity of the disk at some distance  $r > R_d$  from the axis. Thus, the corona is differentially rotating with constant angular velocity on cylinders of equal radius  $r$ ,  $\omega(r) = \text{const}$  (see also Romanova et al. 1998).

We establish the pressure balance on the boundary between the disk and corona such that the disk below this boundary has high density  $\rho_d$  and low temperature  $T_d$ , while corona above this boundary has low density  $\rho_c \ll \rho_d$  and high temperature  $T_c \gg T_d$ . Then we derive the density and pressure distribution in the whole region taking into account the differential rotation of the disk and corona, and force balance between gravitational, pressure, and centrifugal forces (see R02 for details). In the typical density distribution, density in the disk gradually increases outward, while density in the corona decreases while moving to the axis (see Figure 1 of R02). We take the ratios:  $\rho_c/\rho_d = 0.03$  and  $T_d/T_c = 0.03$ . Note, that in two-dimensional simulations we took the ratios,  $\rho_c/\rho_d = 0.01$  and  $T_d/T_c = 0.01$ . We have chosen softer ratios for three-dimensional simulations, in order to get a smaller Alfvén velocity  $v_A = B/\sqrt{4\pi\rho}$ , and larger time-step  $\Delta t \sim \Delta R/v_A$ . Test two-dimensional and three-dimensional simulations with both sets of ratios have shown that in both cases the corona does not influence the disk flow appreciably.

We place the initial inner radius of the disk  $R_d$  at the magnetospheric radius  $r_m$ , where the magnetic pressure of the dipole field balances the matter pressure of the disk,  $p + \rho v^2 = \mathbf{B}^2/8\pi$ . We chose  $B_0$  at this point and  $\rho_d$  such that  $R_d = r_m = 1$ . This choice is based on the fact that we often observe that at small inclination angles the streams always start from the magnetospheric radius  $r_m$  (see also Pringle & Rees 1972; Ghosh & Lamb 1979a,b for theoretical base). This equilibrium was checked numerically in two- and three-dimensional simulations (see R02, and §3.1 of this paper).

We suppose that the star rotates relatively slowly in the sense that its corotation radius is at  $r_{cor} = 3$ . This corresponds to  $\Omega_* = \sqrt{GM/r_{cor}^3} \approx 0.19 = 0.04\Omega_{K*}$ , where  $GM = 1$  in our dimensionless units. For the case of T Tauri stars, this corresponds to a slow rotation rate ( $T \approx 9.4$  days for the parameters used in §2.1 and in R02).

Higher rotation rates including the “propeller” regime will be described in Romanova et al. (2004b).

The *boundary conditions* are similar to those used in K02. At the inner boundary  $R = R_*$ , we take “free” boundary conditions  $\partial/\partial R = 0$  for all variables. This results in the “absorption” of the incoming matter so that there is no standoff shock. Further, the inner boundary is treated as a perfect conductor rotating at the rate  $\boldsymbol{\Omega} = \Omega \hat{\mathbf{z}}$ . In the reference frame rotating with the star the flow velocity is parallel to  $\mathbf{B}$  at  $R = R_*$ . The boundary condition at  $R_*$  on the magnetic field has  $\partial(RB_\phi)/\partial R = 0$ . At the outer boundary  $R = R_{\max}$ , free boundary conditions are taken for all variables. We investigated the possible influence of the outer boundary conditions by running cases where the simulation regions had  $R_{\max} = 4.9, 14, \text{ and } 68$ . We find the same results except for the case  $R_{\max} = 4.9$  where the accretion rate decreases too fast because the reservoir of matter in the disk is too small. Results for the medium and large regions are very close, so that we take  $R_{\max} = 14$  as a standard size of the simulation region.

### 2.3. The Grid and Parallelization of the Code

As mentioned the inner boundary of the simulation region (the “star”) is taken to be at  $R_* = 0.35$ . The size of external boundary depends on the grid (see below).

The spherical grid was inhomogeneous in the  $R$ -direction. The inhomogeneity was such that cells at any distance  $R$  were approximately square with  $\Delta R \sim R\Delta\theta$  for fixed  $\Delta\theta$ . This grid gives a high space resolution close to the star which is important in this problem. At the same time, simulations in a very large region may be performed. The inhomogeneous grid is a smooth analog of nested grids used for example by GBW99.

The angular resolution was taken to be  $N_\theta = 29$  for each block in most cases, and  $N_\theta = 41$  in test cases. The number of points in  $R$ -direction determines the size of the simulation region. The main simulations were done with the radial grid  $N_R = 70$  which corresponds to  $R_{\max} = 14 \approx 40R_* \approx 0.34$  AU. Simulations at the larger grid  $N_R = 96$  corresponding to  $R_{\max} = 68 \approx 194R_* \approx 1.6$  AU were also performed for testing the external boundary conditions.

Note, that each of the six blocks consists of  $70 \times 29 \times 29$  cells. In comparison with a spherical coordinate system, this grid corresponds to  $N_R \times N_\theta \times N_\phi = 70 \times 58 \times 116$ . This grid gives high resolution in the vicinity of the star and inner region of the disk. For the typical grid  $N_\theta = 29$ , the size of the smallest cells near the surface of the star is  $\Delta R = 0.019 \approx 0.053R_*$ . This cell size is 1.7 times larger than in our two-dimensional simulations of the corresponding problem (R02), but about 1.8 times smaller than cells in the innermost grid of GBW99 in their two-dimensional simulations, who had resolution  $\Delta R \approx 0.1R_*$  in the innermost grid. At larger distances from the star, the grid size becomes larger but at the magnetospheric distance  $R = 1$  it is still very small,  $\Delta R \approx 0.1R_*$ , and continues to be sufficiently small in the inner region of the disk  $R \lesssim 5$  which is the most important for our current investigation. At the external boundary,  $R_{\max} = 14$ ,  $\Delta R = 2R_*$ , which is small compared with the disk thickness at this distance. These numbers show that this resolution and grid are sat-

isfactory for three-dimensional simulations of the matter flow around the magnetized star. Note, that in K02 it was shown that even sparser grids such as  $26 \times 15 \times 15$  give satisfactory results.

Fast runs of the three-dimensional code at high grid resolutions become possible due to *parallelization* of the code. First, the code was naturally parallelized to 6 processors, where each of six blocks was assigned to one of six processors. Next, we divided each block into equidistant layers  $N_{layers}$  in  $R$ -direction. Division onto  $N_{layers} = 2, 3, 4, \dots$  etc. allowed us to use  $N_{proc} = 6 \times N_{layers} = 12, 18, 24, \dots$  number of processors. We typically used  $N_{layers} = 8$ , that is, 48 processors. Simulations with larger numbers of processors were also possible and still produced an increase in the computation speed, but the efficiency of using the parallel machine at  $N_{proc} > 48$  declined.

The reported simulations were performed mainly on the fastest V2 nodes of the “Velocity Cluster” at the Cornell Theory Center. Each of the V2 nodes is a dual processor 2.4 GHz Pentium 4 computer. Typical simulations of  $T = 10P_0$  rotations with the grid  $70 \times 29 \times 29$  for each of 6 blocks took approximately 40-50 wall-clock hours on the 48 processors of V2 nodes. This was a reasonable time of simulations in that it allowed us to investigate the three-dimensional flows at different inclination angles (this paper) and other parameters (Romanova et al. 2004b), and to perform test runs with the grid  $70 \times 41 \times 41$ .

## 3. TEST NUMERICAL SIMULATIONS

First, we discuss tests of the code with the above mentioned initial and boundary conditions in hydrodynamic simulations, that is,  $B = 0$ . Secondly, we discuss tests of the code for accretion to a rotating star with an aligned dipole magnetic field,  $\Theta = 0$ . Thirdly, we compare results from our three-dimensional simulations with analogous two-dimensional axisymmetric simulations.

### 3.1. Hydrodynamic Simulations ( $B = 0$ )

Hydrodynamic simulations are important for checking the initial setup of the problem. Simulations were done for grids  $N_1 = 70 \times 29 \times 29$  and  $N_2 = 70 \times 41 \times 41$  for each of six blocks. The first grid was the base grid for subsequent runs with the magnetic field, while the second grid was used for comparisons. Simulations with both grids have shown that the disk-star system stays in equilibrium during many rotations  $T > 15P_0$ , and only slightly evolves due to numerical viscosity. Inward velocity associated with numerical viscosity is very small,  $v \approx 0.001 - 0.003v_{Kd}$ , where  $v_{Kd} = \sqrt{GM/R_d}$  is the Keplerian velocity at the distance  $r = R_d$ . For longer times, the outer regions of the disk become thicker because the grid resolution in that region is relatively low. No high velocities were observed in the corona. The initial differential rotation in the corona was gradually disturbed, and the corona become almost homogeneous but still low-density. The accretion rate to the star was calculated to be  $\dot{M} = 0.01 - 0.02$  in the dimensionless units (see §2.2) for both grids  $N_1$  and  $N_2$ . Note that the accretion rate obtained subsequently in the magnetic cases is about 10 times larger.

Thus, hydrodynamic simulations have shown that the disk-star system stays in the gravity/pressure/centrifugal equilibrium for a sufficiently long time. In three-

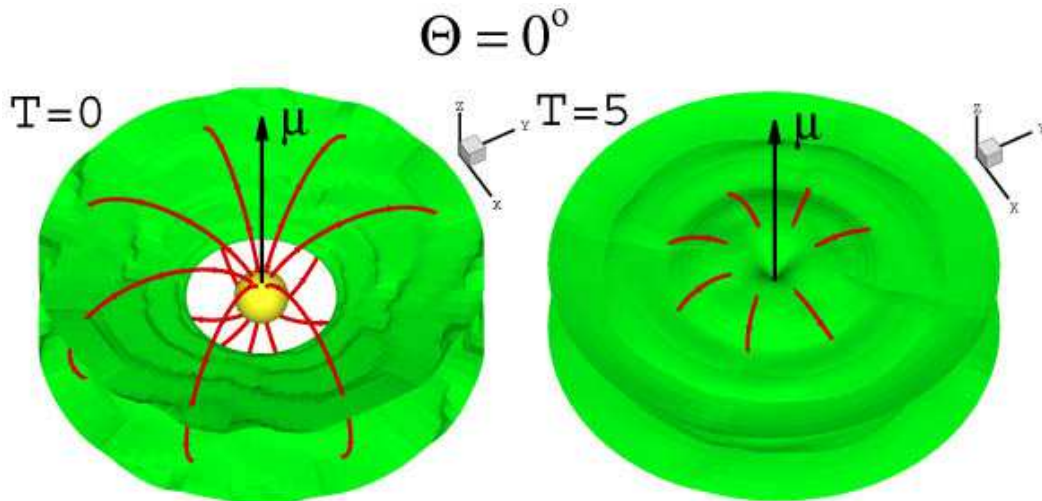


FIG. 2.— The figure shows results of three-dimensional MHD simulations of disk accretion to an aligned rotator ( $\Theta = 0$ ) for  $T = 0$  and  $T = 5$ . Time  $T$  is measured in units of Keplerian rotation period at the inner radius of the disk  $r = R_d = 1$ . The isodensity contours (background) are shown at  $\rho = 0.15$ . The solid lines represent the magnetic field lines. The grid  $70 \times 29 \times 29$  is taken for each of six sectors of the cubed sphere grid. Only part of the simulation region  $R \leq 3$  is shown.

dimensional simulations we were able to follow the evolution during 5 – 12 rotations  $P_0$ . Compared to our two-dimensional simulations (R02) which were followed until  $T > 50$  rotation, here, we do not have viscosity incorporated into the code. Longer simulations with incorporated viscosity will be done in the future research.

In 2D simulations we noticed, that the magnetospheric funnel flow establishes during one rotation period of the inner disk. Subsequently, the flow changes insignificantly during the subsequent 50 rotations and variation depends on the incoming matter flux. In simulations of the accretion to the inclined rotator, we observed that the flow also establishes during the first several rotations, so that as presented in this paper simulations which lasted 5 – 12 rotations are valuable for understanding of 3D funnel flows.

### 3.2. Accretion to an Aligned Rotator, $\Theta = 0$

Next, we performed three-dimensional simulations of accretion to a magnetized star. First, we chose the case where the magnetic axis is perpendicular to the disk and  $\Theta = 0$ . We took the standard parameters for initial and boundary conditions as described in §2.1. We observed that during the first two rotation periods, matter of the disk moved inward, but later it stopped at the magnetospheric radius  $r_m \approx 1 - 1.2$  and went up/down out the disk plane, forming magnetospheric funnel flows. The flow is cylindrically-symmetric, as it should be. The shape of the funnel flow is similar starting from  $T \approx 3$  and during larger  $T$ . Figure 2 shows magnetospheric flow at  $T = 0$  and  $T = 5$ . Here and in subsequent plots we show only the inner part of the simulation region,  $R \leq 3$ , in order to resolve the funnel flow and the inner region of the disk. The magnetospheric flow at  $\Theta = 0$  has a relatively low density, so that we show isocontours at the density level  $\rho = 0.15$ .

The star rotates slowly,  $\Omega_* = 0.04\Omega_{*K}$  with the corotation radius at  $r_{cor} = 3$ . Thus, the magnetic field lines threading the disk at  $r \lesssim 3$  have an angular velocity lower

than the Keplerian, and they transfer negative angular momentum to the disk matter. This leads to the slow inward flow of matter to the star with velocity  $v \approx 0.03 - 0.05v_{Kd}$ . This flow results from the magnetic braking, but the velocity of the flow is much smaller than that obtained using non-equilibrium initial conditions (e.g., Hayashi et al. 1996).

To understand the behavior of the magnetic field, we chose a set of magnetic field lines which initially threaded the disk at a distance  $r \approx 2.8$ , and show the same set of lines at subsequent moments of time. One can see that accreting matter drags these field lines inward. This demonstrates that magnetic field lines are well frozen to the disk. They rotate with the disk in the azimuthal direction and slowly move inward in the radial direction. No opening of magnetic field lines was observed, because the corona right above the disk is matter-dominated (e.g., Romanova et al. 1998).

We should note that the boundary between the disk and magnetosphere of the aligned dipole is a possible site for onset of 3D instabilities, such as the Releigh-Taylor instability which may lead to direct accretion of matter through magnetosphere to the star (see Arons & Lea 1976a,b, Scharlemann 1978). No accretion through 3D instabilities was observed in our simulations. Possibly special simulations are needed with even higher resolution.

### 3.3. Comparison of Two-dimensional and Three-dimensional Simulations

We compared results of axisymmetric three-dimensional simulations with corresponding two-dimensional simulations. Two-dimensional simulations were done in spherical coordinates with the grid  $N_R \times N_\theta = 70 \times 58$  which is the same as the cubed sphere grid  $N_R \times N \times N = 70 \times 29 \times 29$  for each block. Figure 3 shows the meridional cross-sections of matter flow for both cases after  $T = 5$  rotations. Only the inner region  $R < 4.5$  is shown in order to resolve the matter flow around the magnetosphere. One can see that results

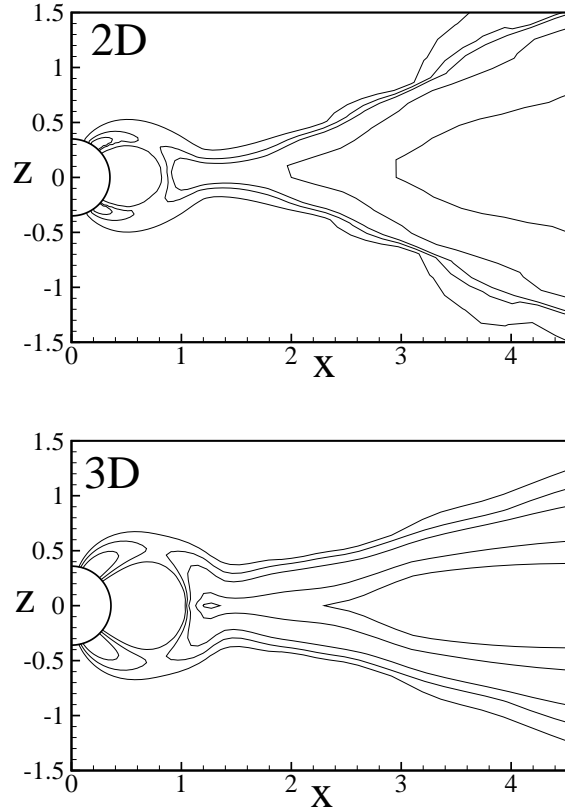


FIG. 3.— Comparison of the density profiles for disk accretion to an aligned rotator obtained from two-dimensional, axisymmetric simulations in spherical coordinates (R02) (top panel), and from three-dimensional simulations in the cubed-sphere coordinates (bottom panel), both at  $T = 5$ .

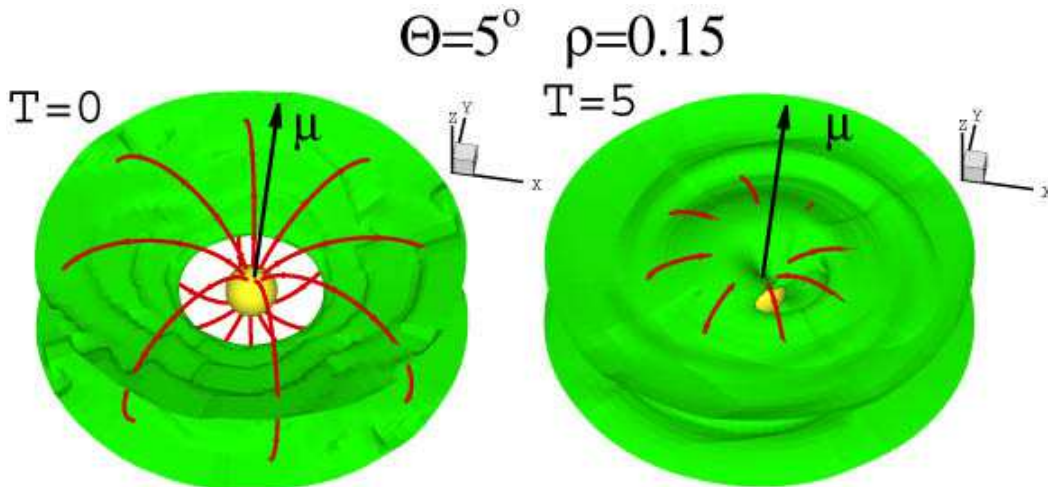


FIG. 4.— Simulations of accretion to an inclined dipole rotator for an inclination angle  $\Theta = 5^\circ$ . Background represents density at the level  $\rho = 0.15$ . Time  $T$  is measured in periods of Keplerian rotation at  $R = 1$ .

of two-dimensional and three-dimensional simulations are qualitatively similar. However, in 3D simulations the magnetosphere radius is  $\sim 10-20\%$  larger than in 2D case: the funnel flow starts at  $r_m \approx 0.9-1.1$  in the two-dimensional simulations and at  $r_m \approx 1.0-1.2$  in the three-dimensional simulations. Besides, the funnel flow in 3D simulations

forms later, after two rotations, compared to one rotation in 2D simulations (R02). These differences seem to be connected with the difference in the accretion rate. Accretion rate in 3D case is about  $\sim 10-20\%$  smaller than in 2D case:  $\dot{M}_{3D} \approx 0.11-0.13$  versus  $\dot{M}_{2D} \approx 0.12-0.16$ . In present simulations the inward accretion of matter oc-

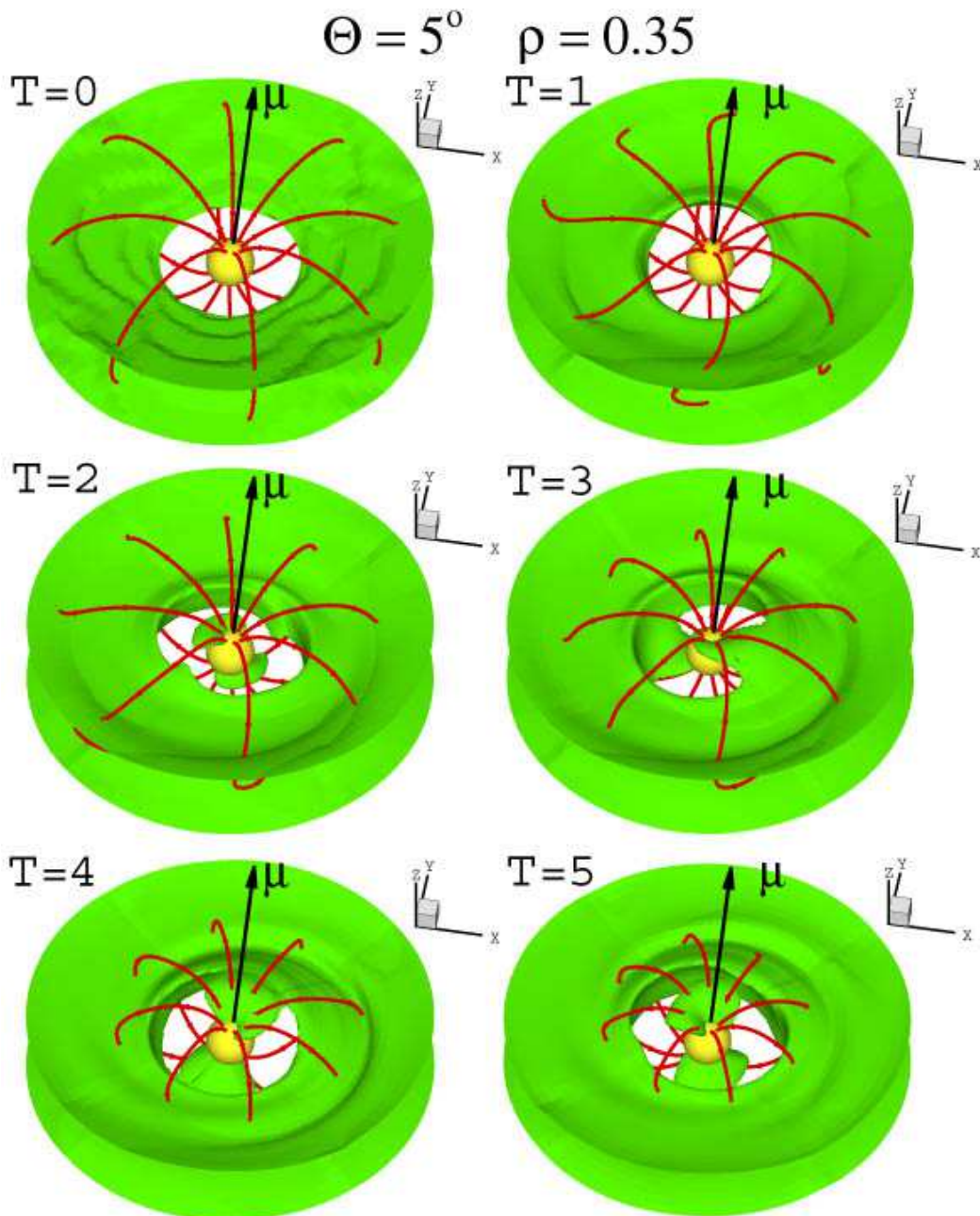


FIG. 5.— Simulations of disk accretion to a misaligned dipole rotator for the case where the dipole moment is inclined by an angle  $\Theta = 5^\circ$ . The background represents the density surface where  $\rho = 0.35$ . Time  $T$  is measured in periods of Keplerian rotation at  $R = 1$ .

curs as a result of small initial magnetic braking (see §2.2). The magnetic braking may have a different nature in 2D and 3D cases which may possibly lead to the observed difference between results in 2D and 3D simulations. In 2D simulations this braking is possibly stronger, which leads to the enhanced accretion compared to 3D simulations.

Here, we should point out that magnetospheric structure does depend on the accretion rate, but *does not* depend on the mechanism of accretion and angular momentum transport. In R02 and in recent 3D simulations (R03), we introduced the simplified  $\alpha$ -type viscosity term to the equations, which permitted us to vary the accretion rate.

In real accretion disks the transport of the angular momentum is connected most probably with magneto-rotational instability (e.g., Balbus & Hawley 1991, 1998). Numerical investigation of this instability needs high space resolution in the disk and typically only part of the disk is considered (e.g., Hawley, Gammie & Balbus 1995; Brandenburg et al. 1995; Stone, et al. 1996; Fleming, Stone, & Hawley 2000). In the present simulations the high grid resolution was set in the vicinity of the dipole, while resolution farther out in the disk was not sufficient to resolve this instability.

These tests provide assurance about the reliability of our three-dimensional MHD code. It is important that at

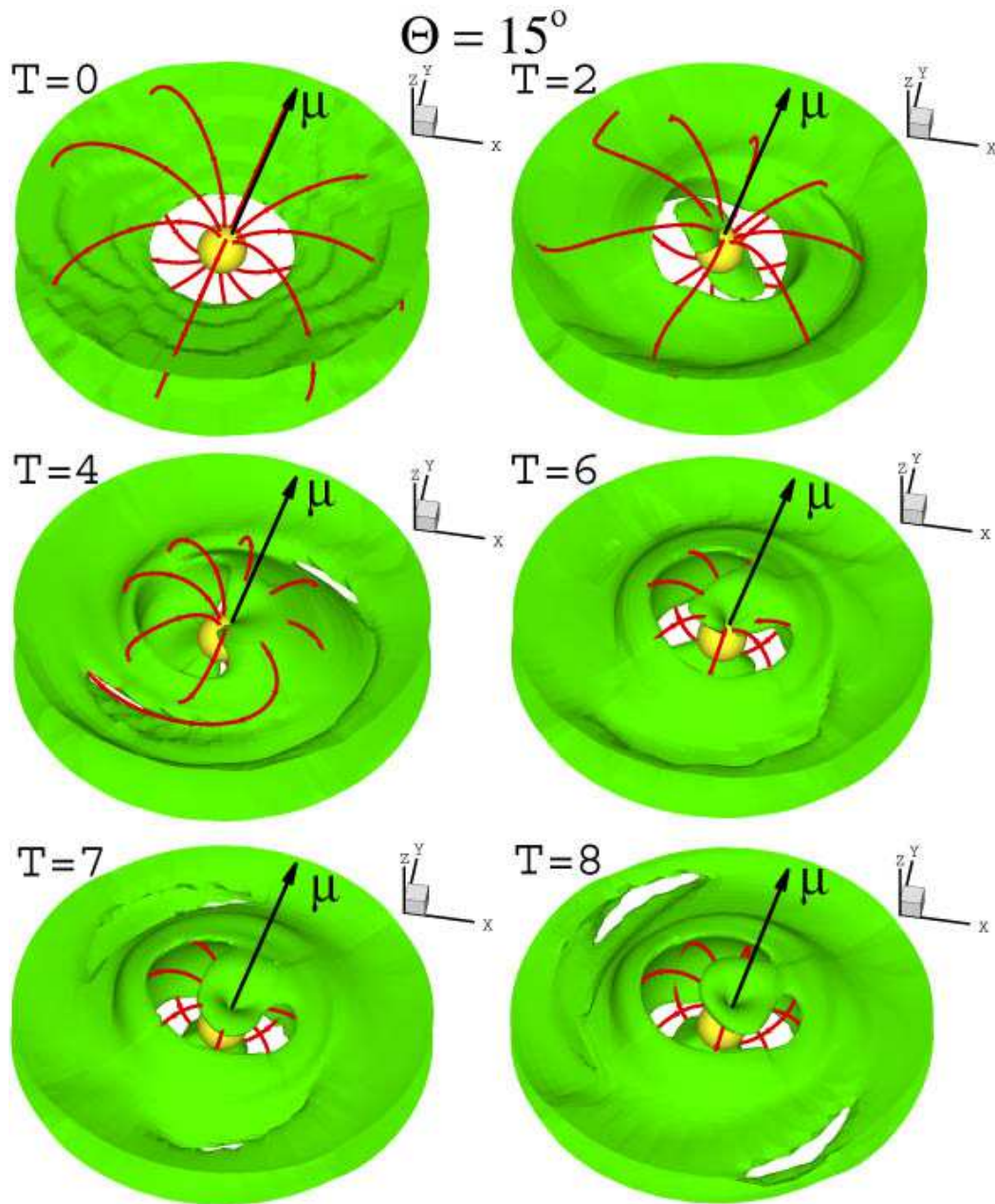


FIG. 6.— Matter flow around an inclined dipole rotator with the dipole inclination angle  $\Theta = 15^\circ$ . The background represents the density isocontours at  $\rho = 0.35$ .

$\Theta = 0^\circ$  the code supports axisymmetry of the flow. We next investigate disk accretion to an inclined dipole rotator.

#### 4. RESULTS OF SIMULATIONS AT DIFFERENT INCLINATION ANGLES $\Theta$

We performed a number of simulations for different inclination angles,  $\Theta = 2^\circ$ ,  $\Theta = 5^\circ$ ,  $\Theta = 15^\circ$ ,  $\Theta = 30^\circ$ ,  $\Theta = 45^\circ$ ,  $\Theta = 60^\circ$ , and  $\Theta = 75^\circ$ . We separately discuss results for small, medium and large inclination angles.

##### 4.1. *Small Inclination Angles: $\Theta = 2^\circ$ , $\Theta = 5^\circ$ and $\Theta = 15^\circ$*

First, it is important to investigate the difference between matter flow at zero,  $\Theta = 0^\circ$ , and *very small* inclination angles. We observed that magnetospheric flow becomes axisymmetric starting from very small inclination angles,  $\Theta = 2^\circ$  and  $\Theta = 5^\circ$ . At such angles, at low density the “windows” of even lower density form in the magnetospheric flow, while at larger densities, matter accretes in two streams.

Figure 4 shows initial state (left panel) and magnetospheric flow at  $T = 5$  (right panel) for relatively low density  $\rho = 0.15$ . One can see that compared to the case with  $\Theta = 0^\circ$  (Figure 2), the windows of lower density form. Windows precess about the rotation axis. The plots are

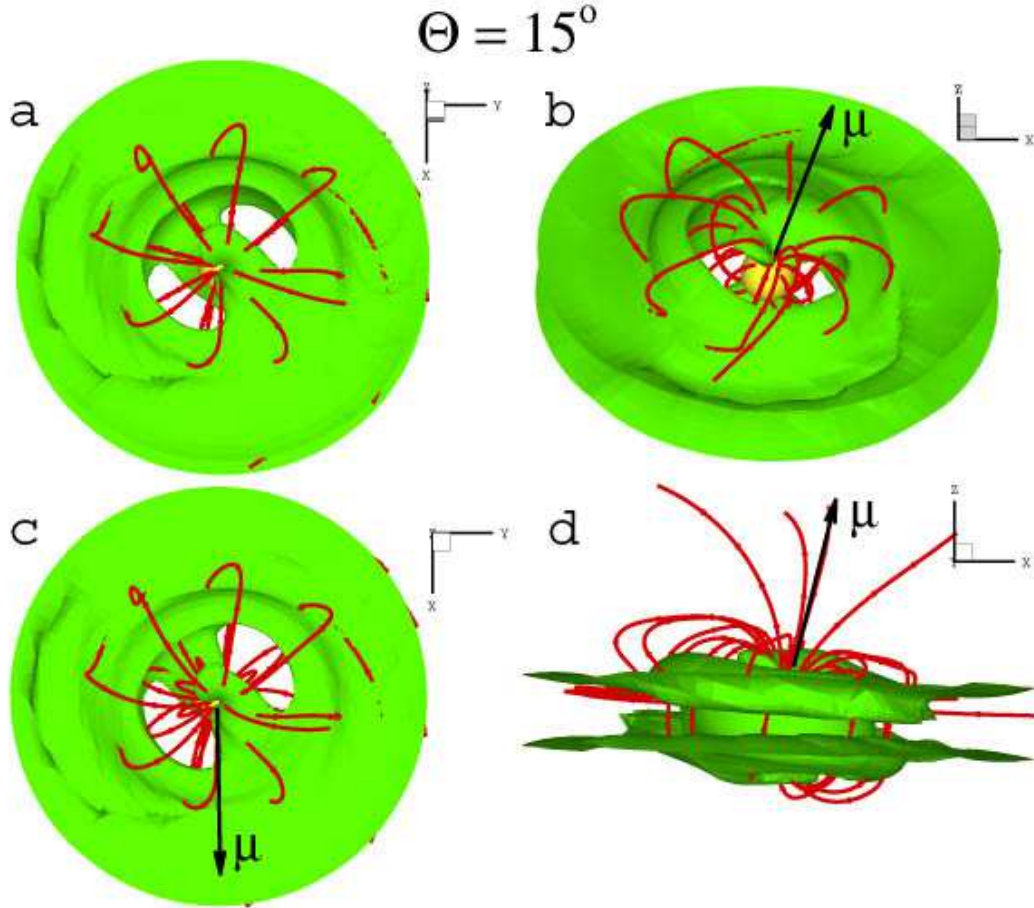


FIG. 7.— The figure shows different projections of the flow for an inclination angle  $\Theta = 15^\circ$  at time  $T = 6$ . The background represents the density at  $\rho = 0.35$ ; the solid lines are magnetic field lines. In panel (a) the  $\mu$  vector is directed towards the observer; in panel (b) the orientation is the same as in Figure 6; panel (c) shows the view along the  $Z$  axis with vector  $\mu$  directed downward; panel (d) shows the side view along the  $Y$  axis.

shown in the coordinate system rotating with the star, and the  $\mu$  vector of the dipole is fixed in the  $(X, Z)$  plane and has the same direction in each of the two plots of Figure 4. Precession of the windows means that its rotation is different from that of the star. Both the star and the disk rotate counterclockwise looking from the  $+z$  pole towards the disk.

The windows rotate in the same direction but faster which means that the period of precession is shorter than that of the star. The faster rotation is due to the fact that inner regions of the disk near the magnetosphere rotate with an angular velocity close to Keplerian  $\omega \approx \Omega_K(r = 1) \approx 1$  while the star rotates slowly with  $\Omega_* \approx 0.19$ . The windows rotate with an angular velocity between these two values.

There is of course a range of densities in the magnetospheric flow. At higher densities,  $\rho \gtrsim 0.15$ , the windows become larger, and at even higher densities,  $\rho \gtrsim 0.3 - 0.4$  matter flows in dense narrow streams. These streams are expected to be important in the occultation of stellar light from an observer. They also form hot spots where they hit the stellar surface.

The area at the star covered by the hot spots depends on density. At  $\rho \approx 0.15$ , hot spots cover  $A_{spots} \approx 40\%$  of

the surface of the star, while at  $\rho \approx 0.3 - 0.4$ , they cover  $A_{spots} \approx 20 - 30\%$  of the surface. At larger densities of the stream, the area is even smaller (see detailed analysis in R03).

Subsequently, we show the high density stream component, but point out that flow pattern is different at the different density levels.

Figure 5 shows the accretion flow at the density level  $\rho = 0.35$ . One can see that after  $T = 2$  rotations two streams form. The azimuthal width of the streams is several times larger than their thickness in the poloidal direction. The streams precess around the  $Z$  axis in the same way as the above mentioned windows. For  $T \gtrsim 5$ , the precession slows, and the streams settle at a specific location about  $30^\circ$  downstream of (counter-clockwise from) the  $(\Omega, \mu)$  plane.

Earlier, we noticed that the streams may follow the longer path along the dipole magnetic field to the star (K02). Now we understand that this is one of the stages of the precession around the  $z$ -axis. Precession slows down because inner regions of the disk come to co-rotation with the magnetosphere (see also §5). The precession may start again if new matter comes to the inner regions of the disk with higher angular momentum. We suggest that if

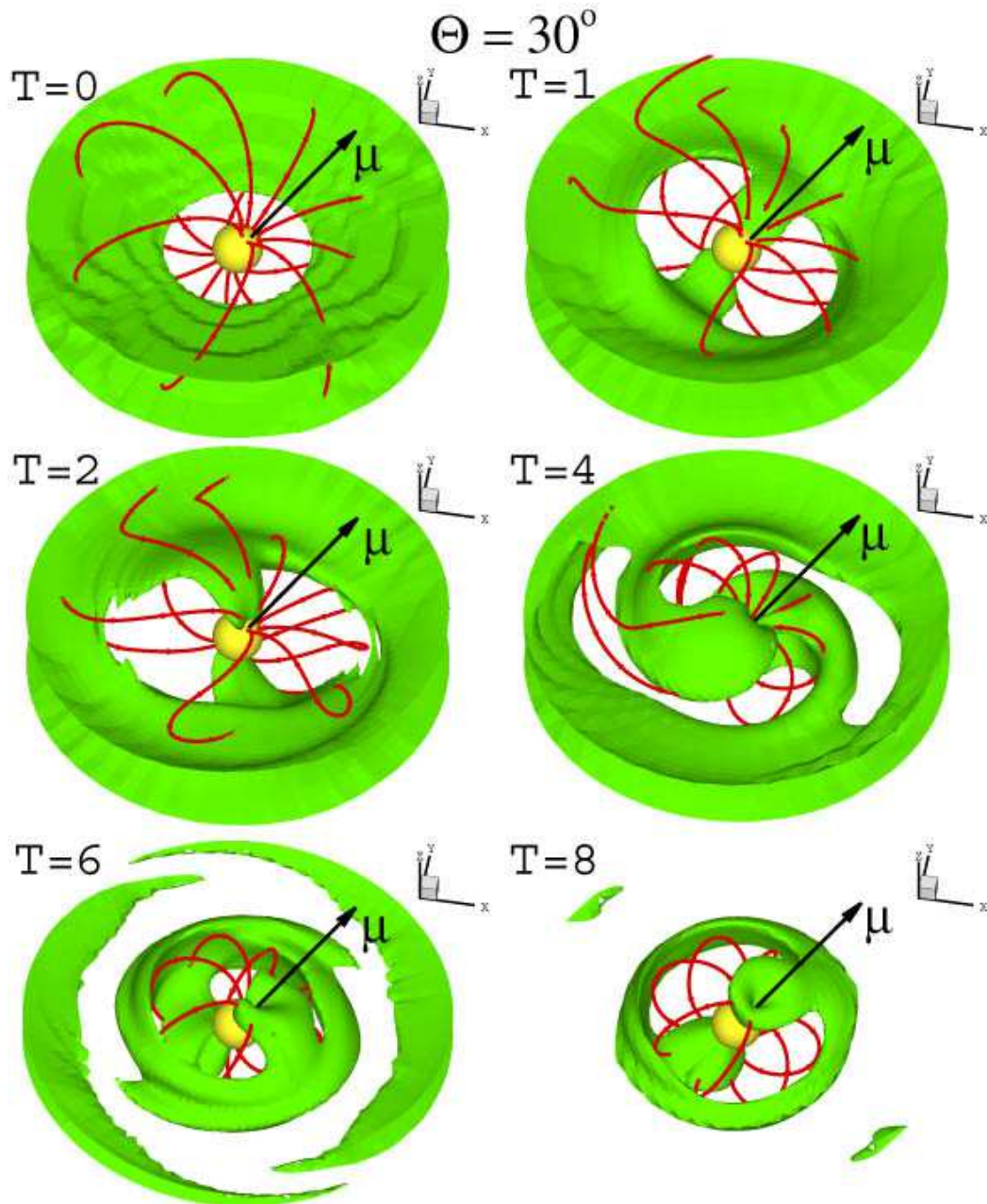


FIG. 8.— Matter flow around the dipole rotator for an inclination angle  $\Theta = 30^\circ$ . The background represents the density isocontours at  $\rho = 0.4$ .

the accretion rate is variable, then this will lead to higher angular velocity of precession (at larger  $\dot{M}$ ) and smaller angular velocity (at lower  $\dot{M}$ ).

Figure 6 shows results of simulations for a larger inclination angle,  $\Theta = 15^\circ$ . One can see that matter again flows to the star along two streams. However, the streams form more rapidly compared to the  $\Theta = 5^\circ$  case, in  $T \approx 1.5$  rotations. They precess around the  $z$ -axis during  $T = 1.5 - 4$ . Later, they settle into a stationary configuration and impact the star at a location downstream or counter-clockwise from the  $(\Omega, \mu)$  plane. Figure 7 shows four projections at  $T = 6$ . Projection (c) shows that the

streams settled at approximately  $30^\circ$  downstream of the  $(\Omega, \mu)$  plane, the same as in the  $\Theta = 5^\circ$  case.

Analysis of forces along the streams has shown that the main lifting force dragging matter up to the streams is the pressure gradient force, while the gravity force is the main one dragging matter along the stream to the star (see more detailed analysis in R03). The magnetic force is negligibly small. Similar forces were observed in analysis of funnel flows in axisymmetric simulations (R02). However, the inclination of the dipole is favorable for lifting: the lifting force can be smaller than in the axisymmetric case.

The favored locations of the streams on the magnetosphere can be understood as follows. Matter in the inner

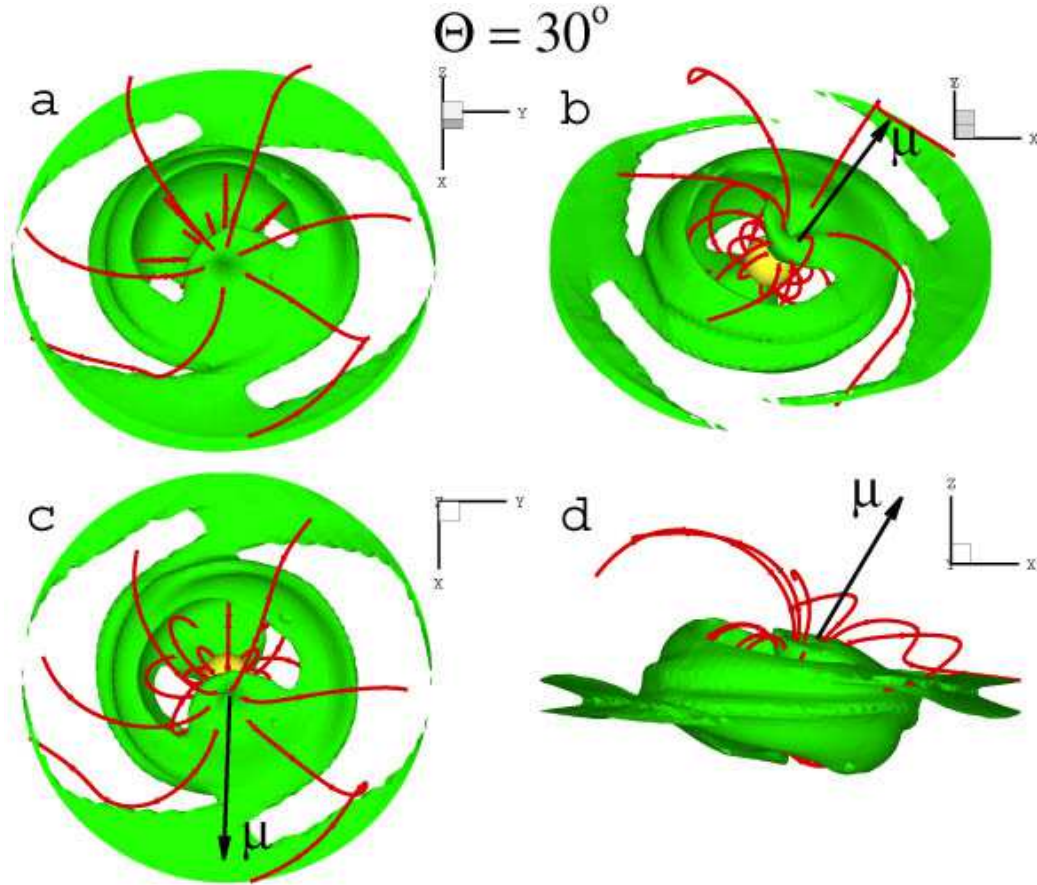


FIG. 9.— The figure shows different projections for an inclination angle  $\Theta = 30^\circ$  and time  $T = 7$ . The background represents density at the level  $\rho = 0.35$ , and the solid lines are magnetic field lines. In panel (a) the magnetic moment  $\mu$  is directed towards the observer; in panel (b) the orientation is the same as in Figure 8; panel (c) shows the view along the  $Z$  axis with  $\mu$  directed downward; and panel (d) shows the side view along the  $Y$  axis.

regions of the disk spirals gradually inward along almost circular orbits. When it comes closer to the magnetosphere, it is subject to magnetic braking. The magnetic braking is the smallest in the  $(X, Z)$  [or,  $(\Omega, \mu)$ ] plane, where the dipole field lines extend to the highest and lowest distances above and below the disk. In the  $(Y, Z)$  plane, the magnetic braking is the largest, because the field lines symmetrically cross the disk at this plane. Thus, matter flows with low braking through the  $(X, Z)$  plane, but is slowed down in the  $(Y, Z)$  plane. From the other side, the poles are closer to the disk matter in the  $(X, Z)$  plane, and magnetic field lines are directed to the poles, so that only small lifting force would be sufficient for the direct accretion to the pole. In the  $(Y, Z)$  plane, matter has much longer path to the poles, and larger lifting force should be applied for accretion in the  $(Y, Z)$  plane. Finally, it seems that matter “prefers” to flow in between of  $(X, Z)$  and  $(Y, Z)$  planes. It is important to note that for the considered slowly rotating star, the inner part of the disk rotates faster than the magnetosphere. Thus the stream settles downstream of (counter-clockwise from) the  $(\Omega, \mu)$  plane. Note, that the location of the stream is different for different values of  $\Omega_*$  (see R03).

Figure 6 shows that for  $T \gtrsim 4$ , magnetic braking leads

to a partial disruption of the disk at  $r < r_{br} \approx 2-3$ . In this region of the disk, the density becomes lower with time. From the other side, matter accumulates near the magnetosphere boundary ( $r_m \approx 1-1.5$ ) forming a “ring”, where the density of the disk increased. Matter from the ring gradually accretes to the star. This matter distribution is similar to that observed in two-dimensional simulations of R02. The difference is that in 3D simulations matter often forms a spiral structure in the area of the magnetic braking  $r < r_{br}$ .

Figures 6 and 7 show that the inner region of the disk becomes asymmetric and the projection (d) shows that inner parts of the disk are “lifted” above the  $Z = 0$  plane of the distant disk. Observations of different cases show that this warp is connected with the tendency of the accreting matter to co-rotate with the magnetosphere. The inner region of the disk is tilted so as to have its normal vector in the direction of the magnetic moment  $\mu$ . This direction of the warp is different from that predicted theoretically (see §1).

Simulations at small inclination angles have shown that *even a small inclination of the dipole moment* leads to non-axisymmetric accretion and possible variability of the light emitted from the surface of the star.

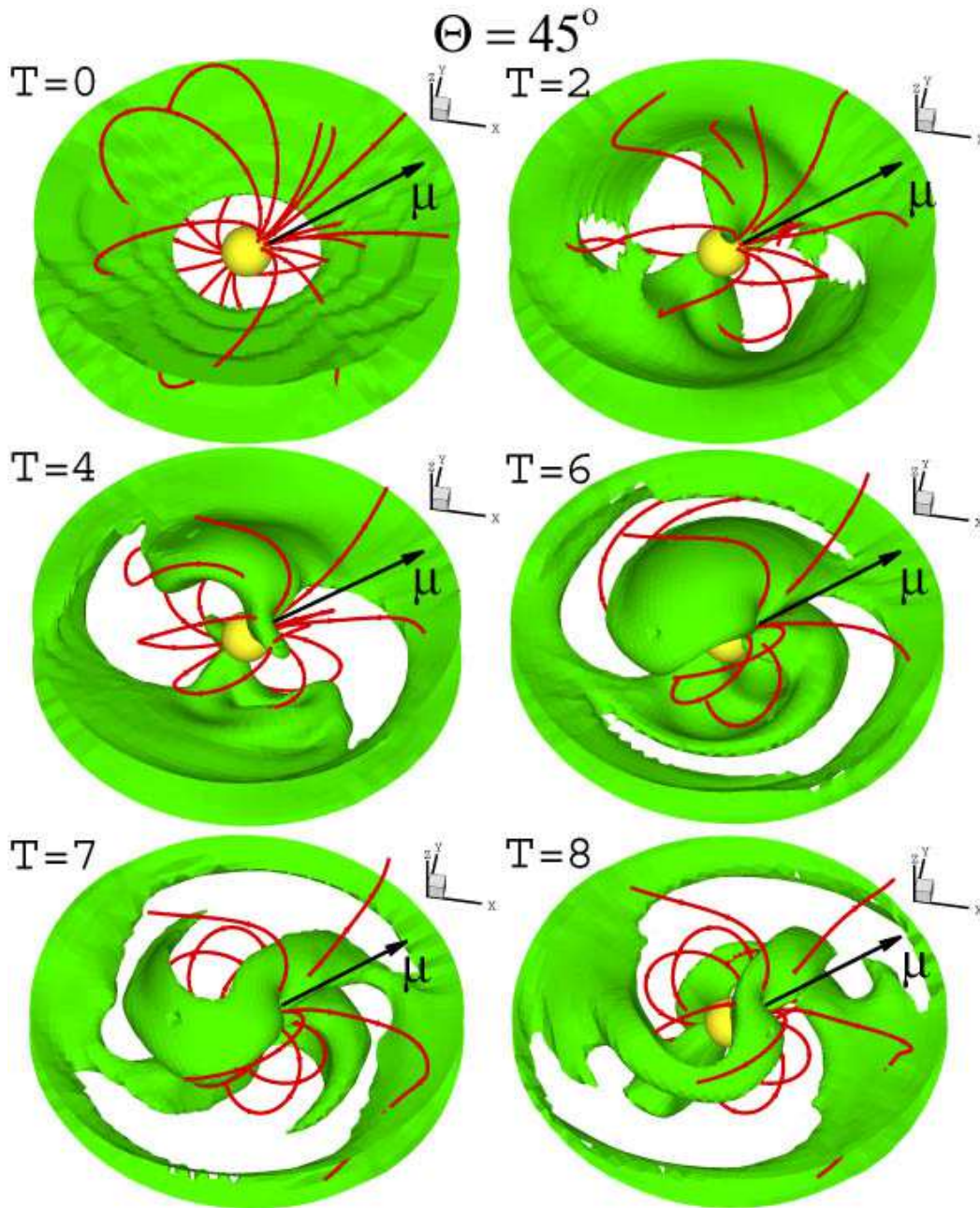


FIG. 10.— Matter flow to an inclined rotator for an inclination angle  $\Theta = 45^\circ$  at the times indicated. The background represents the density surface  $\rho = 0.35$ .

#### 4.2. Medium Inclination Angles: $\Theta = 30^\circ$ and $\Theta = 45^\circ$

Figure 8 shows the matter flow for an inclination angle  $\Theta = 30^\circ$ . We observed that the dense funnel flow streams form faster, after about one rotation. At first, two prominent streams form and precess as in the case of small inclination angles. However, at  $T = 3 - 4$  the magnetic braking starts to disrupt the inner regions of the disk ( $r \lesssim 2 - 3$ ), and the streams turn into leading spirals. We do not bring new matter with Keplerian angular momentum, so that the density in the inner regions of the disk gradually decreases and matter starts to rotate with sub-Keplerian velocity. At the same time, a dense ring forms

around the magnetosphere of the star as in the cases of smaller  $\Theta$ . Later, at  $T \gtrsim 6$ , the density decreased further and a wide gap formed between the inner disk and the star. There is still low density matter between the inner ring and the inner regions of the disk. This structure is similar to that observed in two-dimensional simulations: an inner ring forms around the magnetosphere, and there is a lower density disk around it.

Figure 9 shows different projections at  $T = 6$ . Projection (d) shows that the inner region of the disk is warped. The warp arises from the tendency of the accreting matter to corotate with magnetosphere; that is, the normal to the warped part of the disk tends to align with  $\mu$ .

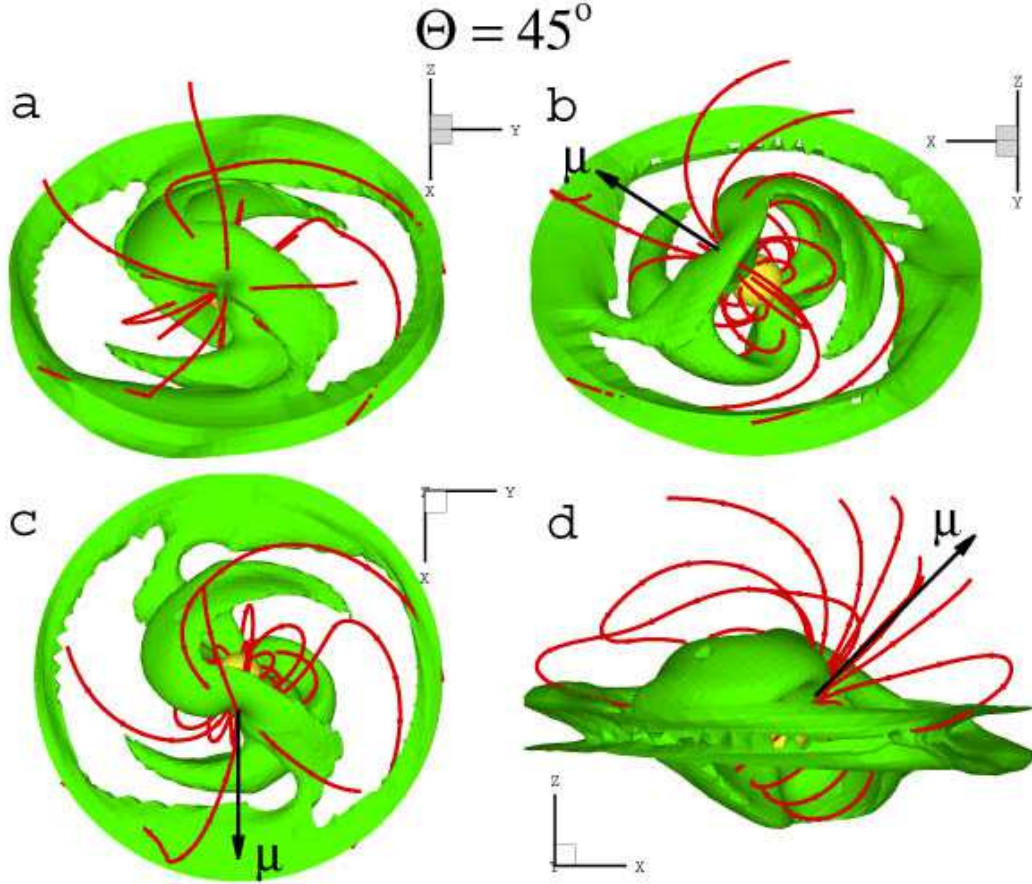


FIG. 11.— Different projections of the accretion flow for inclination angle  $\Theta = 45^\circ$  and time  $T = 7$ . The background represents the density surface  $\rho = 0.35$ , and the solid lines are magnetic field lines. In panel (a) the magnetic moment  $\mu$  is directed towards the observer. Panel (b) shows one interesting projection; panel (c) shows the view along the  $Z$  axis with  $\mu$  directed downward, and panel (d) shows the the side view along the  $Y$ -axis.

Figure 10 shows the accretion flow at  $\Theta = 45^\circ$ . At this relatively large inclination angle, the accreting matter forms a complicated structure with initially two streams as in other cases. But later, four streams form. Inner regions of the disk experience magnetic braking and the disk is significantly disrupted at the chosen density level. However, there is always a bridge of matter connecting external regions of the disk with magnetospheric flow. This bridge is connected with the fact that some matter accretes to the poles “directly” as a result of significant inclination of the dipole. Such multiple streams may give rise to complicated variability of emissions from the stellar surface.

Two sets of magnetic field lines are shown in Figure 10. One set is the same as in Figures 5, 6 and 8. They thread the disk at  $r \approx 2.8$  and are closed inside the region  $r < 3$ . Another set of field lines start closer to the poles. Some of these lines thread the inner regions of the disk due to high inclination of the dipole; others thread the disk far away,  $r \gg 3$ . The field lines threading the disk at close distances, become involved in the disk rotation and form azimuthal magnetic field inside the disk.

Figure 11 shows different projections of the flow for  $\Theta = 45^\circ$  at time  $T = 7$ . The projection (a) shows that the flow is symmetric if the observer looks along the  $\mu$

axis. Projection (c) shows that the streams associated with “direct” accretion to the poles are located at the angle  $\sim 20^\circ - 30^\circ$  downstream (counter-clockwise) from the  $(\Omega, \mu)$  plane as in all above considered cases with smaller  $\Theta$ . Projection (d) shows that magnetospheric flow has a tendency to co-rotate with magnetosphere as found earlier for smaller  $\Theta$ 's. The funnel flows rise high above the disk plane.

#### 4.3. Large Inclination Angles: $\Theta = 60^\circ$ and $\Theta = 75^\circ$

Figure 12 shows the evolution of the matter flow for  $\Theta = 60^\circ$ . The flow becomes complicated after  $T \gtrsim 1$ . From one side, matter accretes directly along field lines to the pole which (at such inclination) is close to the plane of the disk. From the other side, the matter goes around the magnetosphere and accretes through the remote path along the dipole field lines. The combination of these two flows gives a complicated overall flow. At  $T = 7, 8$ , the direct polar flow predominates. However, at  $T = 9$ , more matter came from the disk and matter flow becomes more complicated.

Two sets of magnetic field lines are shown in Figure 12. The number of “polar” field lines threading the inner disk is larger than that at  $\Theta = 45^\circ$  due to the dipole incli-

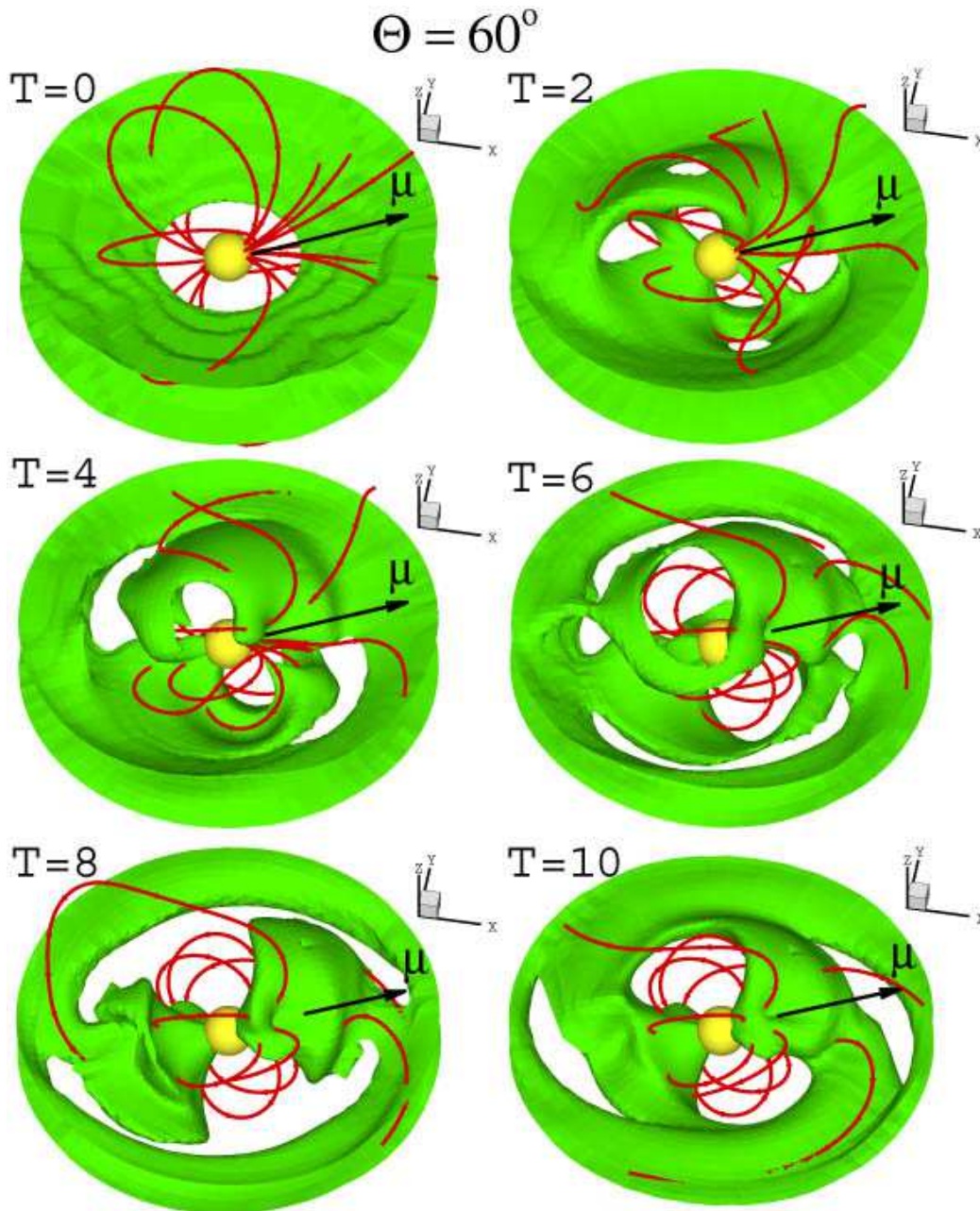


FIG. 12.— Accretion flow to an inclined dipole rotator for an inclination angle  $\Theta = 60^\circ$ . The background represents the density surface  $\rho = 0.35$ .

nation. The magnetic field lines are dragged by the disk forming azimuthal field inside the disk.

Figure 13 shows four projections of the  $\Theta = 60^\circ$  flow at  $T = 8$ . One can see that the flow looks very different at different projections. Projection (c) shows that most of matter accretes through the nearby pole of the inclined dipole. The location of the streams is slightly downstream of the  $(\Omega, \mu)$  plane. Complicated warping is observed which is connected with magnetospheric accretion.

Lastly we discuss the high inclination angle flow with  $\Theta = 75^\circ$ . In this case many “polar” field lines thread the inner region of the disk (see Figure 14 at  $T = 0$ ), while the

closed field lines cross the path of the disk matter. In such a configuration, the disk matter experiences strong magnetic braking, and it accretes to the poles starting from  $T < 1$ . Some matter, however, tries to continue its “circular” path around the star. This matter is lifted up and goes around the magnetosphere, because the closed magnetosphere is on the way. The magnetic field lines which initially were closed inside  $r < 3$ , moved closer to the star dragged by accreting matter as for other  $\Theta$ 's. The “polar” magnetic field lines show complicated bending. Some of them are dragged by the disk, forming an azimuthal field inside the disk.

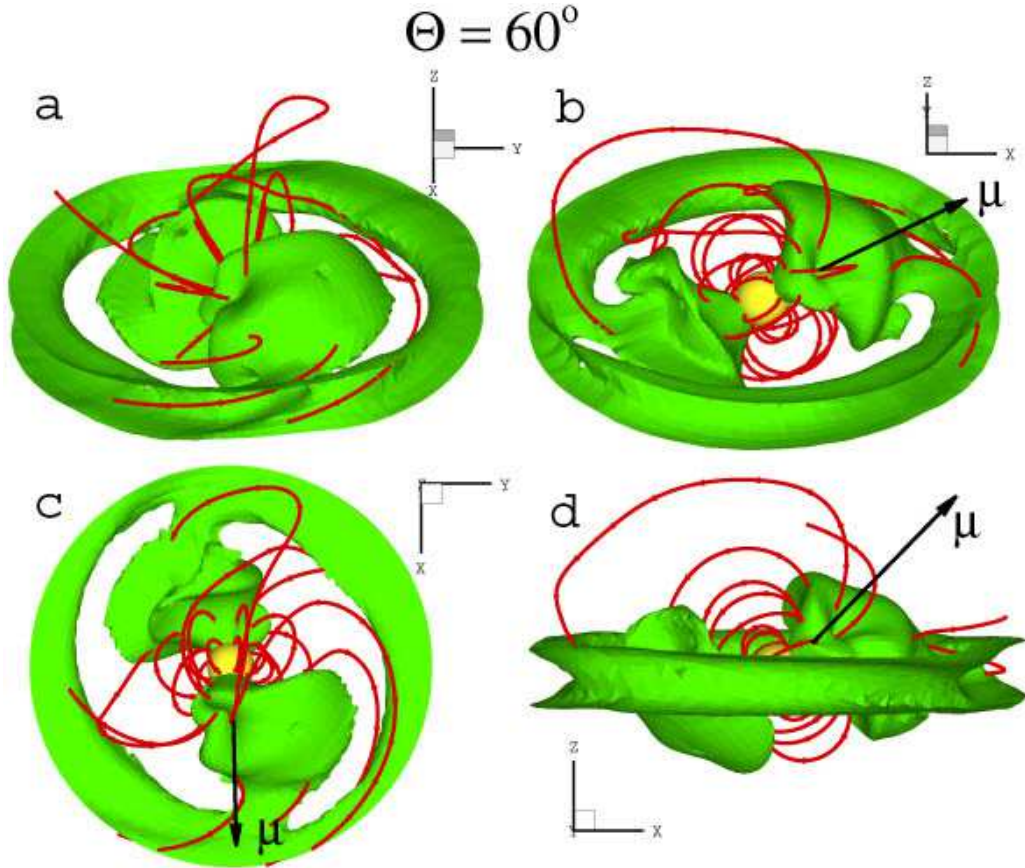


FIG. 13.— Different projections of the accretion flow for an inclination angle  $\Theta = 60^\circ$  at time  $T = 8$ . The background represents the density surface  $\rho = 0.35$ ; the solid lines are magnetic field lines. In panel (a) the magnetic moment  $\mu$  is directed towards the observer; panel (b) shows one of the interesting projections; panel (c) shows view along the  $Z$  axis with  $\mu$  directed downward; and panel (d) shows the the side view along the  $Y$ -axis.

Figure 15 shows projections of the matter flow at  $T = 5$ . Projections (a) and (d) show that matter flowing around the magnetosphere is strongly lifted above the disk plane. These features of the matter flow are typical for a slowly rotating star, where matter in the inner regions of the disk rotates at a higher angular speed than the star and its magnetosphere. Projection (c) shows that the matter streams reach the star downstream of the  $(\Omega, \mu)$  plane as seen in other cases. We conclude that this position of the streams at the magnetosphere is a general feature during accretion to a slowly rotating star (see also panels (c) in Figures 7, 9, 11, 13, and 15). Note that in cases of a faster rotating star (closer to equilibrium) or in the case of a very fast rotating star (“propeller” regime), the location of the streams and their shapes are different (see R03).

#### 4.4. Warping of the Disk

In all of our simulations we observed that the inner regions of the disk are disturbed and become non-axisymmetric. Some parts of the disk are above and others are below the equatorial plane so that the inner disk is warped. In all cases we observed that this warp reflects the tendency of matter to co-rotate with magnetosphere of the star, so that the normal of the inner warped disk has tendency to coincide with the dipole moment  $\mu$ . This

direction of warping does not coincide with any of the proposed theories. Such a warp is specifically noticeable at the Figure 9d, for  $\Theta = 30^\circ$ . This warp has a different nature. It represents the matter flow around the magnetosphere and is not a part of the disk. One can see that matter is warped in the direction of the remote pole.

A possible reason that the observed warp does not coincide with the theory is that most of theories deal with pure diamagnetic disks (e.g., Aly 1980; Lipunov & Shakura 1980). Lai (1999) considered non-diamagnetic and partially diamagnetic disk, but his lifting and precessional forces mainly rely on the twisting of the magnetic field lines, that is on formation of strong  $B_\phi$  component above the disk. We did not observe significant twisting of the field lines in the inner regions of the disk or in the magnetosphere. In the regions of the disk very close to the magnetosphere,  $r_m \lesssim r \lesssim 2 - 3$ , the disk has tendency to corotate with the star. Also, the corona just above the disk has a tendency to corotate with the disk (see also detailed analysis in R02). For this reason the twisting of the magnetic field is small. At larger distances,  $r \gtrsim 3$ , the azimuthal component of the magnetic field may be comparable to the poloidal component. However, these field lines have tendency to be open. Further, the magnetic field in this region is not strong enough to influence the

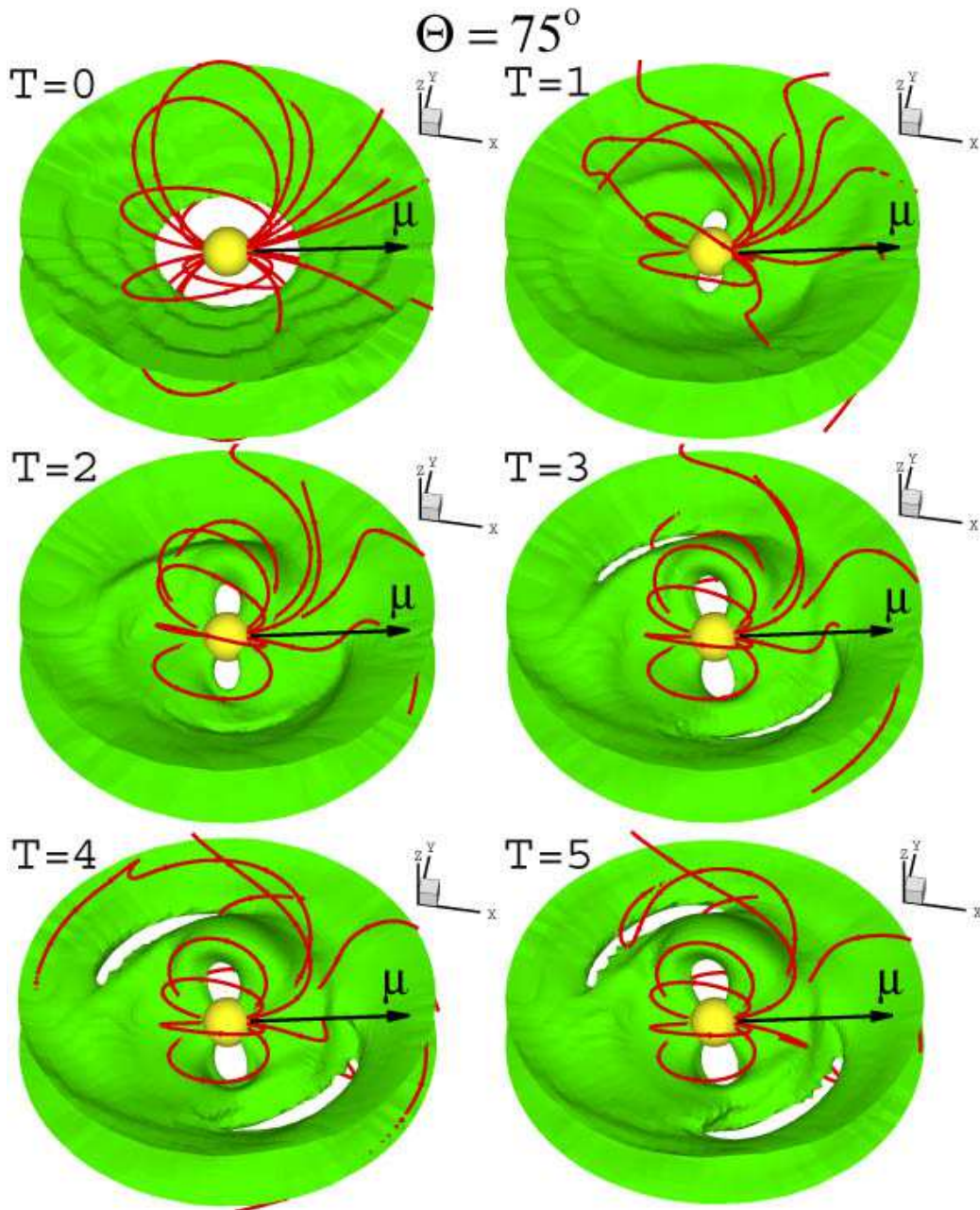


FIG. 14.— Accretion flow to an inclined dipole rotator for an inclination angle  $\Theta = 75^\circ$ . The background represents the density surface  $\rho = 0.45$ .

dynamics of the disk. We conclude that the magnetic field lines threading the inner regions of the disk are not twisted sufficiently to give this type of warping. Further analysis is needed for understanding of warping and asymmetries observed in simulations. Special simulations with a thin diamagnetic disk may be used to check the theory.

##### 5. ANALYSIS OF THE MAGNETIC BRAKING

The simulations show that the interaction of the star's magnetic field with the inner regions of the disk causes a redistribution of density in this part of the disk. The three-dimensional pictures presented above show the magnetospheric flow at fixed density levels. To show the spa-

tial distribution of density, we use two-dimensional slices. We also show one-dimensional distribution of density and angular momentum density along different axes.

To compare results obtained at different inclination angles  $\Theta$ , we take a fixed simulation time. We were able to run some cases longer than others, reaching up to 10–12 rotations in some cases. However, in order to incorporate the case with the highest inclination,  $\Theta = 75^\circ$ , we chose time  $T = 5$  as the reference time for comparing results at different  $\Theta$ .

Figures 16-18 show two-dimensional slices of the density distribution for different inclination angles. Figure 16 shows the slice of the  $(X, Z)$  plane (at  $Y = 0$ ), which co-

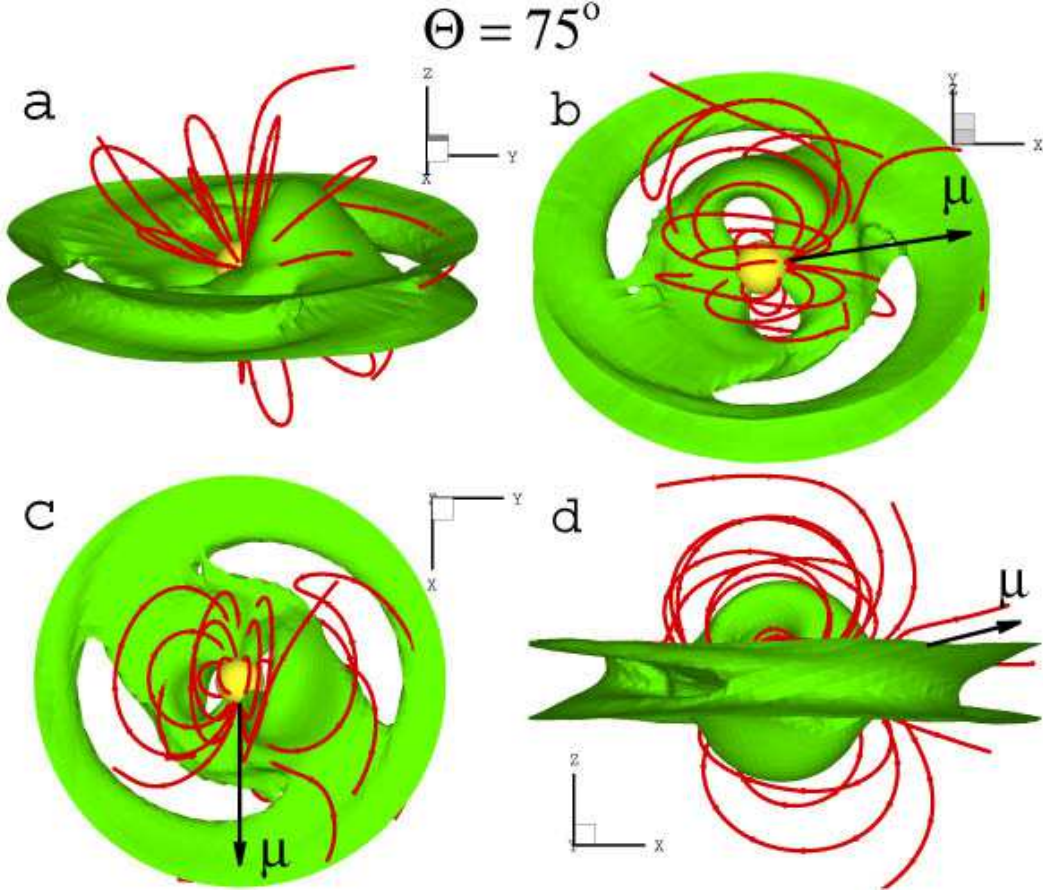


FIG. 15.— Different projections of the accretion flow for an inclination angle  $\Theta = 75^\circ$  and time  $T = 5$ . The background represents the density surface  $\rho = 0.45$ ; the solid lines are magnetic field lines. In panel (a) the magnetic moment  $\mu$  is directed towards the observer; panel (b) shows a projection similar to one in Figure 16; panel (c) shows the view along the  $Z$  axis with  $\mu$  directed downward; and panel (d) shows the side view along the  $Y$ -axis.

incides with the plane containing the magnetic moment (the  $(\Omega, \mu)$  plane). From Figures 16 and 17 it is seen that the external regions of the disk, at  $r \gtrsim 3 - 4$ , are not appreciably disturbed and are approximately the same for different inclination angles  $\Theta$ . Inside this region, however, the scales at which the magnetosphere influences the matter flow are different. Figure 16 shows that for  $\Theta = 5^\circ$ , matter starts to go into funnel flows around the magnetosphere at approximately  $r \approx 1.5$ . For  $\Theta = 15^\circ$ , this occurs at  $r \approx 1.8$ ; at  $\Theta = 30^\circ$ , at  $r \approx 1.9$ . At  $\Theta = 45^\circ$ ,  $60^\circ$ , and  $75^\circ$ , the region is even larger,  $r \approx 2.2$ . Figure 17 shows the density distribution in the  $(Y, Z)$  plane (at  $X = 0$ ). This cross-section also shows that at larger  $\Theta$ , the magnetospheres are larger. Figure 18 shows the  $(X, Y)$  cross-sections ( $Z = 0$ ), which go through the plane of the disk. Figure 18 shows that a relatively high density ring (white color) forms around the low-density magnetospheres at small inclination angles,  $\Theta = 5^\circ$ ,  $15^\circ$  and  $30^\circ$ , but it disappears at larger inclination angles. At very large inclination angles,  $\Theta = 60^\circ$  and  $75^\circ$ , the direct accretion to the poles is observed (white color in the polar regions). This cross-section also shows that the inner region with radii  $R \lesssim 3 - 4$ , has a lower density than the rest of the disk.

We also did *one-dimensional* analysis of the density and angular momentum distribution along the  $X$  and  $Y$  axes. For clarity of the presentation, we divided the inclination angles into two groups: smaller angles,  $\Theta = 0^\circ, 5^\circ, 15^\circ$ , and  $30^\circ$ , and larger angles:  $\Theta = 45^\circ, 60^\circ, 75^\circ$ . The case  $\Theta = 30^\circ$ , was added to the second group for convenience of comparisons. Figure 19a shows density distribution along the  $X$  axis for smaller inclination angles. One can see that the disk is disturbed by magnetic braking for  $r \lesssim 4$ . One can see that at the larger inclination angle the density is smaller. The density is very small for  $X \lesssim 1$ , where the magnetic field is very strong. The strong magnetic field limits the matter flow. At larger  $X$ , the density increases forming a peak of density. This is the ring mentioned earlier, where matter accumulates before accreting to the poles. This feature was the typical one in all two-dimensional simulations (see R02). It is also clearly observed in the simulations at small inclination angles. Figure 19b shows similar distributions along the  $Y$  axis, which are similar to the distributions along the  $X$  axis.

At larger inclination angles,  $\Theta = 45^\circ, 60^\circ$  and  $75^\circ$ , the density distribution is different (see Figures 19c,d). In the  $X$  direction, for  $\Theta = 45^\circ$ , matter comes closer to the stellar surface. For  $\Theta = 60^\circ$  and  $\Theta = 75^\circ$ , the density strongly

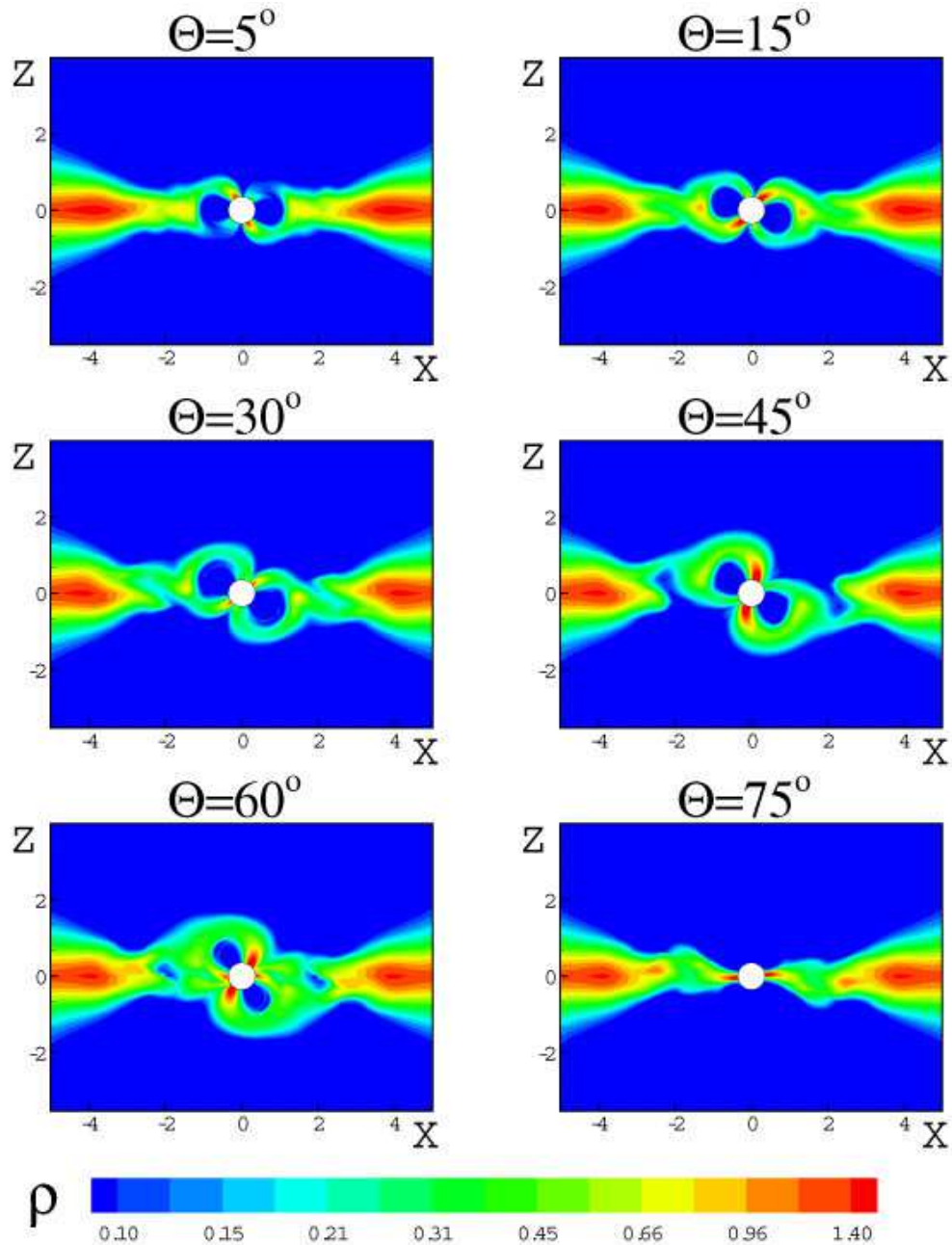


FIG. 16.— The  $(X, Z)$  plane cross-section (in which magnetic moment is located) showing the density distribution at  $T = 5$  for different inclination angles.

increases towards the star, which means that matter accretes directly to the star. The magnetosphere is not an obstacle for the flow at high inclination angles  $\Theta$ . In the  $Y$  direction (see Figure 19d), the matter is stopped by the magnetospheric at a radius  $r \approx 1$  for all inclination angles.

Magnetic braking leads to the deviation of the angular velocity of the matter from the Keplerian value. Figures 20a, b show that at radii  $r \lesssim 3$ , the angular velocity  $\omega$  deviates from Keplerian value starting from  $r \lesssim 3$ . It gradually become smaller than Keplerian and at  $r \lesssim 1.3$  it sharply decreases to the angular velocity of the star  $\Omega_* = 0.19$ . At large inclination angles (see Figures 20c,d) the deviation from Keplerian rotation is much stronger in both the  $X$

and  $Y$  directions. For  $\Theta = 60^\circ$  and  $75^\circ$ , the angular velocity inside the region  $r \lesssim 3$  is  $\omega \approx 0.2 - 0.3$ ; that is, the inner regions of the disk almost co-rotate with the star.

## 6. MATTER AND ANGULAR MOMENTUM FLUXES

Here, we analyze the mass accretion rate to the surface of the star for different inclination angles. Also, we analyze the angular momentum flux to the star and discuss its influence on the angular momentum of the star.

### 6.1. Matter Flux

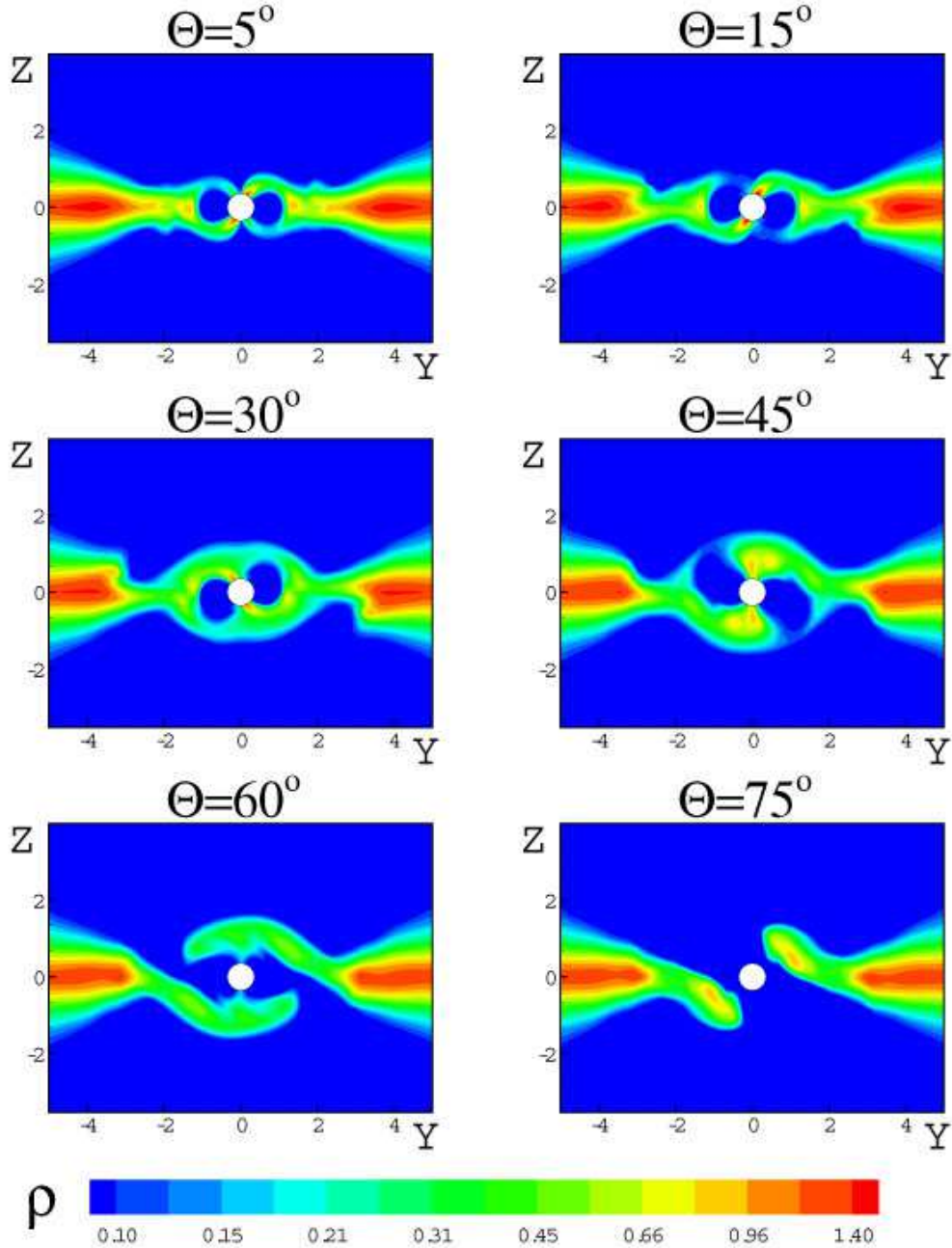


FIG. 17.— The  $(Y, Z)$  plane cross-section showing the density distribution for  $T = 5$  at different inclination angles.

We calculated the matter flux to the surface of the star,

$$\dot{M} = - \int d\mathbf{S} \cdot \rho \mathbf{v} , \quad (5)$$

where the surface integral is taken just outside of the star with  $d\mathbf{S}$  the outward pointing surface area element.

Figure 21 (left panel) shows the matter fluxes at different inclination angles versus time. Initially the accretion rate is zero, but it increases rapidly as matter reaches the surface of the star. It takes less time for larger inclination angles. After the initial rise, the accretion rate settles at a value which changes only slowly, forming the “plateau”. At  $\Theta = 30^\circ$  and  $45^\circ$ , the plateau values of  $\dot{M}$  are approximately the same,  $\dot{M} \approx 0.19$ . At  $\Theta = 60^\circ$ ,  $\dot{M} \approx 0.2 - 0.24$ ,

and at  $\Theta = 75^\circ$  it is even larger,  $\dot{M} \approx 0.26$ . At the smallest inclination angles,  $\Theta = 5^\circ$  and  $\Theta = 15^\circ$ , the  $\dot{M}$  increases gradually and reaches the values  $\dot{M} \approx 0.19 - 0.2$ , but it is not clear, whether the plateau was formed or not. Note, that at  $\Theta = 0^\circ$ , the accretion rate is smaller,  $\dot{M} \approx 0.13$ , but not significantly smaller than that for inclined rotators. These values of  $\dot{M}$  are in accord with two-dimensional axisymmetric simulations done with a similar grid,  $\dot{M} \approx 0.14 - 0.16$ . Note, that simulations in the hydrodynamic case ( $B = 0$ ) lead to a much smaller accretion rate  $\dot{M} \approx 0.02$ . This accretion is due to the small numerical viscosity as discussed in the Section 2. Thus, we

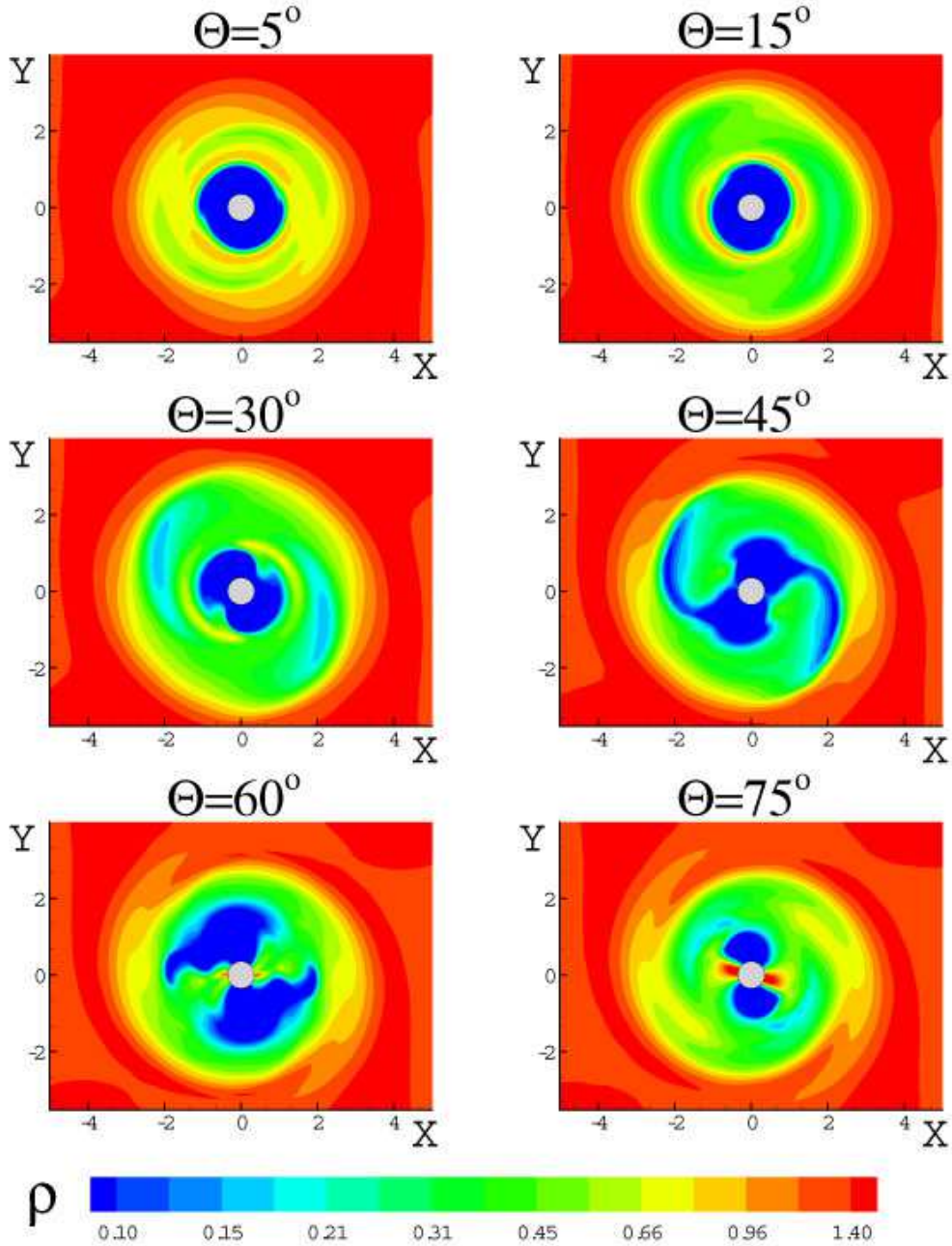


FIG. 18.— The  $(X, Y)$  plane cross-section showing the density distribution at  $T = 5$  for different inclination angles.

conclude that the accretion rate is larger at larger  $\Theta$  because the magnetic braking is larger at larger  $\Theta$ .

### 6.2. Torque on the Star

Incoming matter and the magnetic field carry in or remove angular momentum from the star. The angular momentum of this matter is much less than that of the star during the time span of the simulations. Thus, we fix angle  $\Theta$  and direction and value of  $\Omega$ . We calculate torques relative to different axes which carry information about possible long-term evolution of the star.

The total angular momentum flux in the reference frame rotating with the star  $(X, Y, Z)$  consists of the part carried by the matter which gives the matter torque,  $\mathbf{N}_m$ ,

and that carried by the field which gives the field torque  $\mathbf{N}_f$ ,

$$\mathbf{N} = \mathbf{N}_m + \mathbf{N}_f = - \int d\mathbf{S} \cdot \mathbf{v} \rho (\mathbf{r} \times \mathbf{u}) + \frac{1}{4\pi} \int d\mathbf{S} \cdot \mathbf{B} (\mathbf{r} \times \mathbf{B}), \quad (6)$$

where the integration is over a spherical surface just outside of the star with  $d\mathbf{S}$  the outward pointing surface area element, and where  $\mathbf{u}$  is the velocity in the inertial frame and  $\mathbf{v}$  is the velocity in the frame rotating with the star. For an inclined rotator,  $\mathbf{N}$  is not in general along a particular axis. Denoting  $\mathbf{L}$  the angular momentum of the star, we have

$$\frac{d\mathbf{L}}{dt} = \frac{d^*\mathbf{L}}{dt} + \Omega \times \mathbf{L} = \mathbf{N} \quad (7)$$

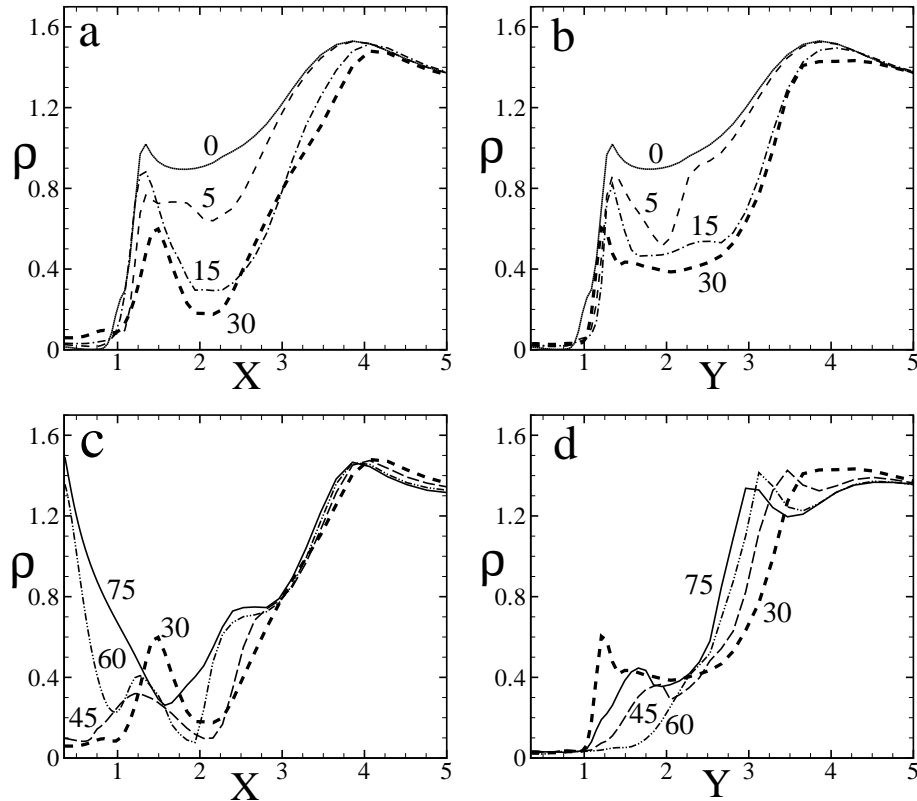


FIG. 19.— Density distribution along the  $x$  (left panels) and  $y$  (right panels) axes for inclination angles  $\Theta = 0^\circ, 5^\circ, 15^\circ, 30^\circ$  (top panels) and  $\Theta = 30^\circ, 45^\circ, 60^\circ, \&75^\circ$  (bottom panels).

where  $d/dt$  is with respect to an inertial reference frame and  $d^*/dt$  is with respect to the rotating  $(X, Y, Z)$  coordinate system. For the considered case, the angular momentum of the star and that of the incoming matter in the disk have the same direction. Therefore, the direction of  $\mathbf{L}$  averaged over the star's rotation period remains in the  $z$  direction of the inertial or laboratory reference frame.

We observed that in the vicinity of the star the angular momentum flux is carried predominantly by the magnetic field. The flux carried by the matter is very small, about 1% of the total. Far from the magnetosphere, the angular momentum flux is carried mainly by the matter. With decreasing distance, the matter transfers its angular momentum to the magnetic field. A similar behavior was observed in axisymmetric simulations (R02).

The torque about the  $Z$  axis,  $N_z$ , is responsible for spinning-up or spinning-down of the star. Positive  $N_z$  corresponds to spinning-up of the star. Figure 21 (right panel) shows the flux  $N_z$  for different inclination angles. In the present work the star rotates slowly so that the incoming matter spins-up the star. The variation of  $N_z$  is analogous to the variation of  $\dot{M}$  (Figure 21, left panel). One can see, that initially, the magnetic braking was large for all inclination angles, but later it decreased and became relatively constant. At small inclination angles,  $\Theta = 0^\circ, 5^\circ$  and  $15^\circ$ , the torque went to an approximately constant value rapidly,  $T < 0.5$ . The torque is almost constant for  $\Theta = 0^\circ, 5^\circ$ , and decreases only slowly at  $\Theta = 15^\circ$ . At large  $\Theta$ , the  $N_z$  decreases gradually. If new matter is accreted to the inner regions of the disk, then  $N_z$  will stay at

some non-zero level, as we observed in our two-dimensional simulations (R02). Additional simulations with steady accretion from the disk are needed to resolve the difference in angular momentum transport at different  $\Theta$ .

A positive torque  $N_x$  would, in the absence of the  $\boldsymbol{\Omega} \times \mathbf{L}$  term, act to shift the star's angular momentum  $\mathbf{L}$  in the  $+X$  direction, that is towards the direction of  $\boldsymbol{\mu}$ . However, the  $\boldsymbol{\Omega} \times \mathbf{L}$  is expected to be important for an actual, oblate star where the moments of inertia are  $I_z > I_x = I_y$  with  $(I_z - I_x)/I_x \ll 1$ . For this reason a torque  $N_x$  acts to give  $\Omega_y = N_x / (I_x \Omega_z \Omega_{prec})$  which corresponds to a very slow precession of the  $\boldsymbol{\Omega}$  about  $\mathbf{L}$  which is fixed in space, where  $\Omega_{prec} = (I_z - I_x) \Omega_z / I_x$  is the free precession angular frequency. Figure 22 (left panel) shows the torque  $N_x$  for different inclination angles  $\Theta$ . One can see, that at  $\Theta = 0$ ,  $N_x = 0$ , which confirms that our three-dimensional code supports axisymmetry with high accuracy. This also confirms that the origin of this momentum is connected with interaction of the *inclined* dipole with the disk. Even at small inclination angle,  $\Theta = 5^\circ$ , the torque  $N_x$  is non-zero. It varies sinusoidally and changes sign from negative to positive and back, and settles to a positive value. For  $\Theta = 30^\circ$ , variations of larger amplitude were observed. At inclination angles,  $\Theta = 45^\circ$  and  $60^\circ$ ,  $N_x$  is initially negative, but becomes positive later. A negative torque at  $\Theta = 75^\circ$  gradually increases to larger values.

A positive torque  $N_y$  would, in the absence of the  $\boldsymbol{\Omega} \times \mathbf{L}$  term, act to shift the star's angular momentum  $\mathbf{L}$  in the  $+Y$  direction, that is towards the direction of  $\boldsymbol{\Omega} \times \boldsymbol{\mu}$ . However, as mentioned the  $\boldsymbol{\Omega} \times \mathbf{L}$  is expected to be important

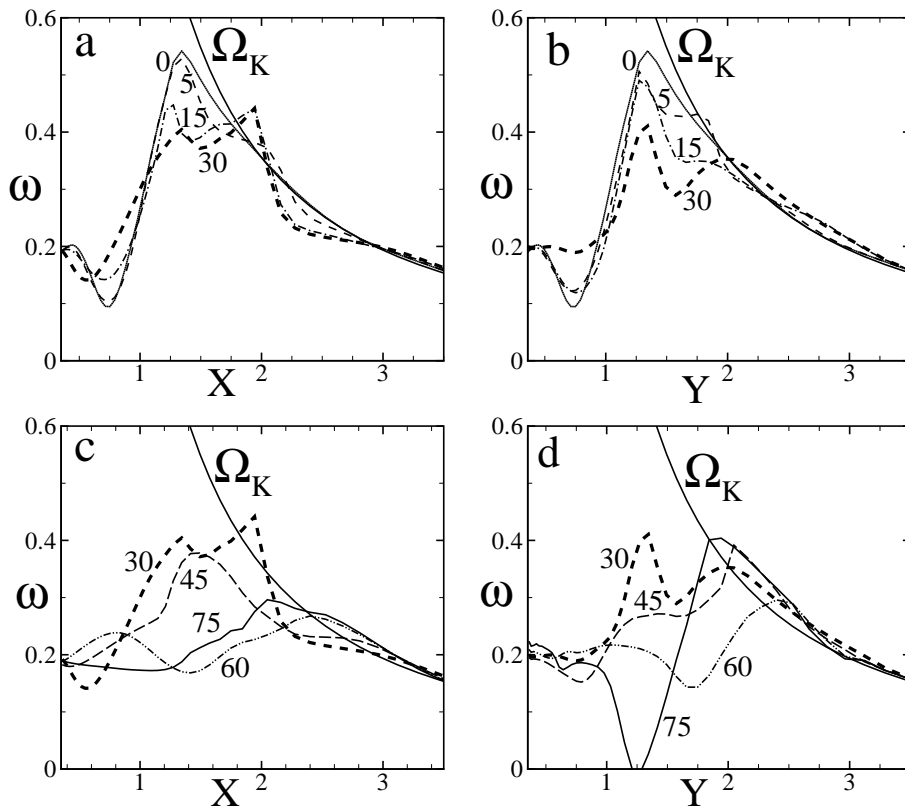


FIG. 20.— Angular velocity distribution along the  $X$  axis (left panels) and  $Y$  axis (right panels) for inclination angles  $\Theta = 0^\circ, 5^\circ, 15^\circ, 30^\circ$  (top panels) and  $\Theta = 30^\circ, 45^\circ, 60^\circ, \& 75^\circ$  (bottom panels).

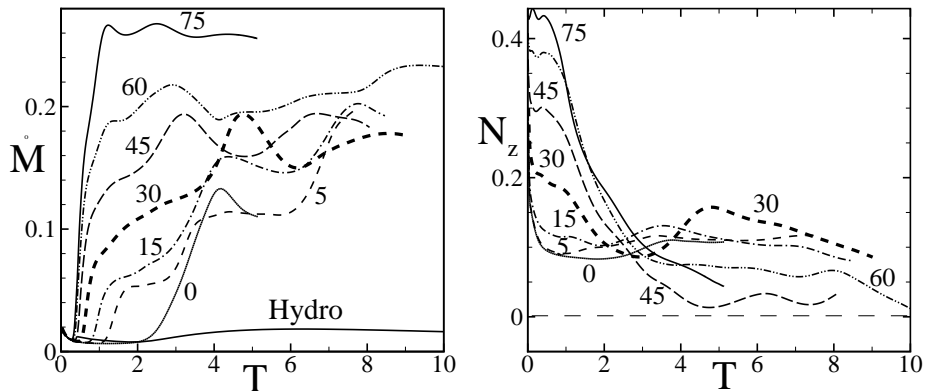


FIG. 21.— The left-hand panel shows the matter flux to the star  $\dot{M}$  versus time  $T$  for different inclination angles  $\Theta$ . The right-hand panel shows torque  $N_z$  versus time at different  $\Theta$ .

for an actual, oblate star. For this reason a torque  $N_y$  acts to give  $\Omega_x = -N_y / (I_x \Omega_z \Omega_{prec})$  which corresponds to a very slow precession of the  $\Omega$  about  $\mathbf{L}$  which is fixed in space. Figure 22 (right panel) shows the torque  $N_y$  for different inclination angles. We observed that for  $\Theta = 0$ ,  $N_y = 0$ , as it should be. At the small inclination angle  $\Theta = 5^\circ$ ,  $N_y$  varies around zero value, which is connected with the formation of two streams which precesses around the magnetosphere of the star. At  $\Theta = 15^\circ$ , the sign of  $N_y$  is mainly negative, though variations of the flux are also observed. At  $\Theta = 30^\circ$  and  $\Theta = 60^\circ$ , the initial variation of the flux at  $T \lesssim 2$  has the same value,  $N_y \approx -0.18$ . How-

ever, later both fluxes decreased to smaller values. Note that at  $\Theta = 30^\circ$ , the  $N_y$  changes sign to positive values. For  $\Theta = 75^\circ$ , the torque  $N_y$  goes to an approximately constant value  $\approx -0.07$ .

We emphasize that for more rapidly rotating stars, the torques may behave quite differently from the case of the slowly rotating star considered here.

## 7. CONCLUSIONS AND OBSERVATIONAL CONSEQUENCES

We performed full three-dimensional ideal MHD simulations of disk accretion to a slowly rotating star with an inclined dipole magnetic field for different inclination

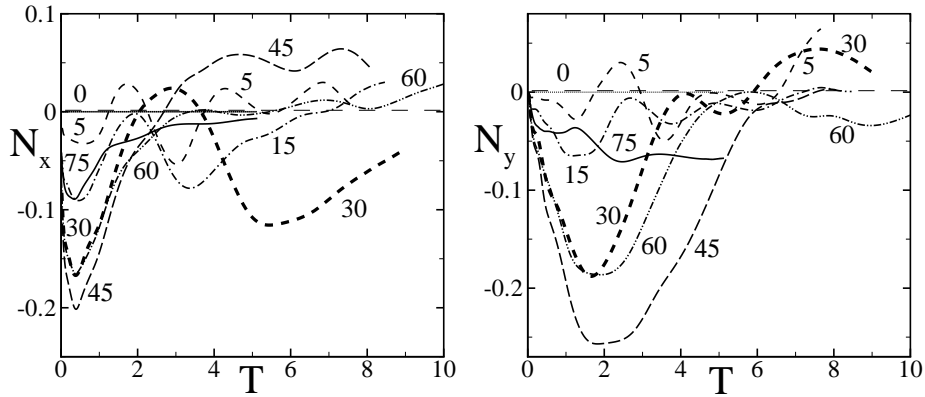


FIG. 22.— Torque on the star along the  $X$  axis (left panel) and  $Y$  axis (right panel) at different inclination angles  $\Theta$ .

angles  $\Theta$ . Below, we summarize the main results of the simulations (§7.1) and discuss possible observational consequences (§7.2).

### 7.1. Main Results of Numerical Simulations

In the following we summarize the main results and conclusions of our simulations.

1. We observed that the accretion flow near the star becomes non-axisymmetric at very small inclination angles,  $\Theta \sim 2^\circ - 5^\circ$ .

2. The shape of magnetospheric flow depends on the density. At a sufficiently low density, most of the volume of the magnetosphere is filled by matter, excluding small “windows” of even lower density. At a higher density, the matter is in two or several “accretion streams.”

3. For relatively small inclination angles,  $\Theta \lesssim 30^\circ$ , the densest matter accretes in *two streams*. The streams typically follow a path to the closest magnetic pole of the star with displacement of  $20^\circ - 30^\circ$  downstream (counter-clockwise) from the  $(\Omega, \mu)$  plane on the star’s surface.

The accretion streams may precess about the star’s rotation axis. The precession appears to be caused by incoming matter with higher than average angular momentum; this matter causes the streams to rotate faster than the star. In periods of steady accretion, the streams do not precess. Precession is observed more often in cases with small  $\Theta$ .

For intermediate inclination angles,  $30^\circ \lesssim \Theta \lesssim 60^\circ$ , the magnetospheric flow consists of two or more streams. Several streams (typically four) is a common feature for  $\Theta = 45^\circ$ , while in other cases ( $\Theta = 30^\circ$ ,  $\Theta = 60^\circ$ ) several streams appear in periods of enhanced accretion. The number of streams may depend on the density level.

For large inclination angles,  $\Theta \gtrsim 60^\circ$ , matter typically accretes in two streams. However, the streams have a different shape compared with those at small  $\Theta$  and they come to the star near the equatorial plane.

4. The density distribution is close to that observed in two-dimensional simulations (R02). Namely, magnetic braking leads to depression of density in the region  $r_m \lesssim r \lesssim 4$  and to the formation of a dense ring near the magnetospheric boundary,  $r \sim r_m$ . Formation of a dense ring is typical for  $\Theta \lesssim 30^\circ$ . At larger  $\Theta$ , the ring does not form, and for  $\Theta \gtrsim 60^\circ$ , matter accretes to the star through equatorial streams (see Figures 16-18).

Magnetic braking leads to a significant departure of the angular velocity of the disk from Keplerian in the region  $r \lesssim 2 - 3$ . For  $\Theta = 60^\circ$  and  $\Theta = 75^\circ$ , the region of the disk out to  $r \approx 2.5$  almost co-rotates with the star (see Figure 20c,d).

5. The inner regions of the disk are often warped. This warp forms because matter leaving the disk, start to move around magnetosphere, thus forming a flow with axis close to that of  $\mu$ . The region between the undisturbed disk and the matter which co-rotates with magnetosphere has a warped shape. However, it has a different nature compared to that predicted by theory of warped disks (see §4.4).

6. The angular momentum transport to the star was investigated. For the considered small angular velocity of the star, the angular momentum flux relative to the  $Z$  axis gives a positive torque  $N_z$  which acts to spin-up of the star for all  $\Theta$ . Angular momentum is transported to the surface of the star by the magnetic field (as observed in our two-dimensional simulations, R02) The matter carries about 1% of the total angular momentum flux near the surface of the star.

The torques  $N_x$  and  $N_y$  were calculated in the reference frame corotating with the star. They give information about the long term evolution of the star’s angular momentum  $\mathbf{L}$ , and of  $\Omega$  and  $\mu$ . For typical accretion rates ( $\sim 10^{-7} - 10^{-9} M_\odot/\text{yr}$  for a protostellar system), the angular momentum of the star changes by a negligible amount during a rotating period of the inner region of the disk. This justifies our having  $\Theta$  fixed in the simulations.

### 7.2. Observational Consequences

The described simulations are important for understanding the physics of accreting magnetized stars, for example, CTTs, cataclysmic variables, and X-ray pulsars. The simulations provide a basis for understanding the photometric and spectral variability the stars. Radiation in different spectral bands may be associated with different regions, the stellar surface, hot/cold spots on the stellar surface, and the magnetospheric plasma. Knowledge of the magnetospheric flow is essential to interpreting observed light curves, spectra, and temporal variations in the spectra. The presented simulations may allow the estimation of  $\Theta$  in different systems, and may help to establish the

main source of the radiation in different wavebands. Some of predictions from this work are:

1. Non-axisymmetric accretion and the formation of accretion streams (which give hot spots on the star's surface) is expected in almost all stars, because the limiting angle  $\Theta$  at which non-axisymmetry appears is small ( $\Theta \sim 2^\circ$ ).

2. At a fixed  $\Theta$ , the geometry of the magnetospheric flow is different at different density levels. At a sufficiently low density, all space is occupied by matter at this or larger densities. At a larger density level, "windows" appear in the accretion flow, and at even larger densities, matter accretes along narrow accretion streams. The variability of different spectral lines and of different wavebands of the continuum radiation is expected to depend on the density, temperature and velocity distributions along the line of sight to the star. Variation of the accretion rate may also change the pattern of variability, because at the same  $\Theta$  the number of streams may temporarily change. Spiral structure may appear in the inner regions of the disk.

3. If the light curve has features with variability equal to approximately a half of the main period, this may be a sign of two rotating hot/cold spots, or, a sign of occultation of stellar light by two magnetospheric streams. If the light curve suggest occultations, then the inclination angle predicted by simulations is relatively small,  $\Theta < 30^\circ$ . Relatively short periods (few rotations) of the multi-stream features may appear, but most of the time the two-stream features will dominate. Different observations point to such a possibility (e.g., Muzerolle, Hartmann & Calvet 1998, Petrov et al. 2001).

4. If the light curve indicates precession of the accretion streams, then the simulations point to the likelihood

that the inclination angle is small,  $\Theta \lesssim 10^\circ$ . The variability pattern for two precessing streams is characterized by an initial period smaller than the half-period  $P/2$ , and a subsequent regular increase of period to  $P/2$ . This type of variability may be rare because at small inclination angles, the expected amplitude of variability is small.

5. If the light curve shows a quasi-period much shorter than the period of rotation of the star (say,  $\sim 1/4P$ ), then it will be a sign of multiple streams which are typical for intermediate inclination angles,  $30^\circ < \Theta < 60^\circ$ . Recently Muzerolle, Calvet, & Hartmann (2001), suggested that some observations of CTTs may be explained if the funnel flows have a multiple stream geometry.

6. At large inclination angles,  $\Theta \gtrsim 60^\circ$ , matter also accretes in two streams, but they are located close to the equatorial plane. In such a case variability may be connected with occultation of stellar light by the warped disk (as proposed by Bouvier et al. 1999, 2003). The light curves are expected to be different from those where occultation by magnetospheric streams dominate.

This research was conducted using the resources of the Cornell Theory Center, which receives funding from Cornell University, New York State, federal agencies, foundations, and corporate partners. This work was supported in part by NASA grants NAG5-9047, NAG5-9735, and by NSF grant AST-9986936. AVK and GVU were partially supported by INTAS CALL2000-491 grant and by Russian program "Astronomy." J.V.W. was supported by DOE cooperative agreement DE-FC03-02NA00057. The authors thank Dr. Stinchcombe for editing the manuscript.

#### REFERENCES

- Agapitou, V., Papaloizou, J.C.B., & Terquem, C. 1997, MNRAS 292, 631
- Aly, J.J. 1980, *Astron. & Astrophys.*, 86, 192
- Arons, & Lea 1976, ApJ, 207, 914
- Arons, & Lea 1976a, ApJ, 210, 792
- Balbus, S.A., & Hawley, J.F. 1991, ApJ, 376, 214
- Balbus, S.A., & Hawley, J.F. 1998, *Rev. Mod. Phys.*, 70, 1
- Bardou, A., & Heyvaerts, J. 1996, A&A, 307, 1009
- Bertout, C., Basri, G., & Bouvier, J. 1988, ApJ, 330, 350
- Bildsten, L., et al. 1997, ApJS, 113, 367
- Bouvier, J. & Bertout, C. 1989, A&A, 211, 299
- Bouvier, J., Chelli, A., Allain, S., etc. 1999, A&A, 349, 619
- Bouvier, J., Grankin, K.N., Alencar, S.H.P., et al. 2003, A&A, in press
- Brandenburg, A., Nordlund, A., Stein, R.F., & Torkelsson, U. 1995, ApJ, 446, 741
- Camenzind, M. 1990 in: *Rev. Mod. Astron.* 3, ed. G. Klare, Springer-Verlag (Heidelberg), 234
- Deeter, J.E., et al. 1998, ApJ, 502, 802
- Feigelson, E.D., & Montmerle, T. 1999, ARA&A, 37, 363
- Fendt, C., & Elstner, D. 2000, *Astron. Astrophys.* 363, 208
- Fleming, T.P., Stone, J.M., & Hawley, J.F. 2000, 530, 464
- Ghosh, P., & Lamb, F.K. 1979a, ApJ, 232, 259
- Ghosh, P., & Lamb, F.K. 1979b, ApJ, 234, 296
- Goodson, A.P., Bhm, K.-H., Winglee, R. M. 1999, ApJ, 524, 142
- Hartmann, L., "Accretion Processes in Star Formation", Cambridge University Press, 1998
- Hawley, J.F., Gammie, C.F., & Balbus, S.A. 1995, ApJ, 440, 742
- Hayashi, M.R., Shibata, K., & Matsumoto, R. 1996, ApJ, 468, L37
- Herbst, W. et al. 1986, ApJ, 310, L71
- Hirose, S., Uchida, Y., Shibata, K., & Matsumoto, R. 1997, PASJ, 49, 193
- Johns, C.M., & Basri, G. 1995, ApJ, 449, 341
- Horn, S., & Kundt, W. 1989, Ap&SS, 158, 205
- Koldoba, A.V., Lovelace, R.V.E., Ustyugova, G.V., & Romanova, M.M. 2002a, *Astron. J.*, 123, 2019
- Koldoba, A.V., Romanova, M.M., Ustyugova, G.V., & Lovelace, R.V.E. 2002b, ApJ, 576, L53
- Königl, A. 1991, ApJ, 370, L39
- Küker, Henning, Rüdiger 2003, ApJ, in press
- Lai, D. 1999, ApJ, 524, 1030
- Li, J. & Wickramasinghe, D.T. 1997, M.N.R.A.S., 286, L25
- Lipunov, V. M., Semenov, E.S., & Shakura, N.I. 1981, *Sov. Astron.*, 25, 439
- Lipunov, V. M., & Shakura, N.I. 1980, *Sov. Astron. Lett.*, 6, 14
- Livio, M. & Pringle, J.E. 1992, MNRAS, 259, 23
- Lovelace, R.V.E., Romanova, M.M., & Bisnovatyi-Kogan, G.S. 1995, MNRAS, 275, 244
- Miller, K.A. & Stone, J.M. 1997, ApJ, 489, 890
- Muzerolle, J, Calvet, N., & Hartmann, L. 2001, ApJ, 550, 944
- Muzerolle, J, Hartmann, L., & Calvet, N. 1998, ApJ, 116, 455
- Ostriker, E.C., & Shu, F.H. 1995, ApJ, 447, 813
- Powell, K.G., Roe, P.L., Linde, T.J., Gombosi, T.I., & De Zeeuw, D.L. 1999, *J. Comp. Phys.*, 154, 284
- Petrov, P.P., Gahm, G.F., & Gameiro, J.F. et al., 2001, A&A, 369, 993
- Pringle, J.E., & Rees, M.J. 1972, A&A, 21, 1
- Romanova, M.M., Ustyugova, G.V., Koldoba, A.V., & Lovelace, R.V.E. 1998, ApJ, 500, 703
- Romanova, M.M., Ustyugova, G.V., Koldoba, A.V., & Lovelace, R.V.E. 2002, ApJ, 578, 420
- Romanova, M.M., Ustyugova, G.V., Koldoba, A.V., & Lovelace, R.V.E. 2004a, submitted to ApJ
- Romanova, M.M., Ustyugova, G.V., Koldoba, A.V., & Lovelace, R.V.E. 2004b, ApJ, in preparation
- Ronchi, C., Iacono, R., & Paolucci, P.S. 1996, *J. Comp. Phys.* 124, 93
- Scharlemann, E.T. 1978, ApJ, 219, 617
- Safier, P.N. 1998, ApJ, 494, 336
- Sheffer, E.K., et al. 1992, *Sov. Astron.*, 36, 41
- Shu, F.H., Najita, J., Ruden, S.P., & Lizano, S. 1994, ApJ, 429, 797 (S94)
- Smirnov, D.A., Fabrika, S.N., Lamzin, S.A., & Valyavin, G.G. 2003, A&A, 401, 1057
- Stone, J.M., Hawley, J.F., Gammie, C.F., Balbus, S.A. 1996, ApJ, 463, 656

- Terquem, C., & Papaloizou, J.C.B. 2000, *Astron. & Astrophys.*, 360, 1031
- Trümper, J., Kahabka, P., Ögelman, H., Pietsch, W., & Voges, W. 1986, *ApJ*, 300, L63
- Wang, Y.-M. 1995, *ApJ*, 449, L153
- Warner, B. 1995, *Cataclysmic Variable Stars* (Cambridge: Cambridge Univ. Press)
- Warner, B. 2000, *The Publications of the Astronomical Society of the Pacific*, Volume 112, Issue 778, p. 1523
- Wickramasinghe, D. T., Wu, K., & Ferrario, L. 1991, *MNRAS*, 249, 460